Geophysical Journal International

Geophys. J. Int. (2012) **189,** 1430–1456 doi: 10.1111/j.1365-246X.2012.05455.x

Wavelet-based directional analysis of the gravity field: evidence for large-scale undulations

M. Hayn,[1] I. Panet,[2,3] M. Diament,[3] M. Holschneider,[1] M. Mandea[4] and A. Davaille[5]

[1]*Institute for Mathematics, University of Potsdam, Am Neuen Palais* 10, 14469 *Potsdam, Germany. E-mail: hayn@math.uni-potsdam.de*
[2]*Institut National de l'Information Geographique et Forestiere (formerly Institut Geographique National), Laboratoire de Recherche en Geodesie, GRGS, ENSG,* 6/8, *av. Blaise Pascal, Cite Descartes, Champs/Marne,* 77455 *Marne-la-Vallee Cedex* 2, *France*
[3]*Institut de Physique du Globe de Paris (IPGP, Sorbonne Paris Cite, UMR* 7154 *CNRS, Universite Paris Diderot), Bat. Lamarck, Case* 7011, 35, *rue Helene Brion,* 75205 *Paris Cedex* 13, *France*
[4]*Centre National d'Etudes Spatiale,* 2, *place Maurice Quentin,* 75039 *Paris, France*
[5]*Laboratoire FAST (CNRS/Univ. P-Sud/UPMC) Batiment* 502, *rue du Belvedere, Campus Universitaire,* 91405 *Orsay, France*

Accepted 2012 March 9. Received 2012 January 25; in original form 2011 January 22

SUMMARY

In the eighties, the analysis of satellite altimetry data leads to the major discovery of gravity lineations in the oceans, with wavelengths between 200 and 1400 km. While the existence of the 200 km scale undulations is widely accepted, undulations at scales larger than 400 km are still a matter of debate. In this paper, we revisit the topic of the large-scale geoid undulations over the oceans in the light of the satellite gravity data provided by the GRACE mission, considerably more precise than the altimetry data at wavelengths larger than 400 km.

First, we develop a dedicated method of directional Poisson wavelet analysis on the sphere with significance testing, in order to detect and characterize directional structures in geophysical data on the sphere at different spatial scales. This method is particularly well suited for potential field analysis. We validate it on a series of synthetic tests, and then apply it to analyze recent gravity models, as well as a bathymetry data set independent from gravity. Our analysis confirms the existence of gravity undulations at large scale in the oceans, with characteristic scales between 600 and 2000 km. Their direction correlates well with present-day plate motion over the Pacific ocean, where they are particularly clear, and associated with a conjugate direction at 1500 km scale. A major finding is that the 2000 km scale geoid undulations dominate and had never been so clearly observed previously. This is due to the great precision of GRACE data at those wavelengths. Given the large scale of these undulations, they are most likely related to mantle processes. Taking into account observations and models from other geophysical information, as seismological tomography, convection and geochemical models and electrical conductivity in the mantle, we conceive that all these inputs indicate a directional fabric of the mantle flows at depth, reflecting how the history of subduction influences the organization of lower mantle upwellings.

Key words: Wavelet transform; Satellite geodesy; Gravity anomalies and Earth structure; Pacific Ocean.

1 INTRODUCTION

Since the analysis of orbit perturbations of the first artificial satellites that allowed the pioneering global mapping of the gravity field at low resolution, the investigation of the geoid made large progress and brought significant advances in understanding our planet's interior. Among the most prominent results, global analyses of geoid models together with topography and seismology data shed light upon the viscosity variations of the Earth's mantle (e.g. Hager *et al.* 1985; Hager & Richards 1989; Ricard & Wuming 1991; Forte & Mitrovica 2001). In the eighties, the advent of satellite altimetry revolutionized the knowledge of the gravity field in the oceans, revealing many features previously unknown, such as uncharted submarine seamounts (e.g. Haxby *et al.* 1983; Baudry & Diament 1987; Baudry *et al.* 1987) and undulated patterns in the geoid. The discovery of these lineations was one of the most impressive results of satellite altimetry. Geoid undulations of amplitude between 10 and 20 cm and wavelength around 200 km, roughly oriented in the direction of plate motion, have thus been reported in the Pacific, Indian and South Atlantic oceans (Haxby & Weissel 1986; Cazenave *et al.* 1987; Fleitout *et al.* 1989). Different mechanisms have been proposed to explain these features, such as a small-scale

mantle convection layer beneath the lithosphere of a fast-spreading ocean, promoted by a low-viscosity layer (Buck & Parmentier 1986; Robinson & Parsons 1988), lithospheric boudinage due to asymmetric slab pull forces (Dunbar & Sandwell 1988), magmatic traces of former mantle plumes (Fleitout & Moriceau 1992) and the effect of thermal stresses due to the progressive cooling of the lithosphere from top to bottom (Sandwell & Fialko 2004).

At longer wavelengths, geoid undulations have also been reported in different areas, but authors disagree on their dominant wavelength. Haxby & Weissel (1986) mentioned undulations of scales up to 500 km, located mostly over the older parts of the plates. Cazenave *et al.* (1992) observed dominant wavelengths of 750 to 1100 km, elongated in an east-west direction over the Pacific ocean. Undulations of wavelengths of 400 to 500 km were evidenced by Maia & Diament (1991) with higher amplitudes on older lithosphere, results which coincide with those by Haxby & Weissel (1986). According to Baudry & Kroenke (1991), geoid undulations of amplitudes up to 50 cm and wavelengths between 400 and 600 km can be found about 1200 km west of the East Pacific Rise (EPR) in the South Central Pacific, roughly parallel to the plate motion. Wessel *et al.* (1994) showed that the alignment of these large-scale undulations with the direction of the Pacific plate motion has a series of maxima for several wavelengths between 150 and 1400 km, very close to mantle discontinuities, which suggests that these large-scale patterns might be related to the mantle structure. In all these studies, wavelengths larger than 1400 to 2000 km are removed from the data in a preliminary step, and the data processing was based on Fourier transforms and filters in one and two dimensions. Only Wessel *et al.* (1994) used another method, computing the correlations with oriented axisymmetric sinusoids, but in doing so they lost information on the localization of the undulations.

With the advent of satellite gravity, and the launch of the GRACE mission in 2002, data of unprecedented quality have become available at wavelengths down to 200 km and again revolutionized our view on the Earth's gravity field (Tapley *et al.* 2004). Whereas satellite altimetry-derived gravity anomalies are best determined at wavelengths smaller than ∼200 km, GRACE data are extremely precise at longer wavelengths, in the waveband where large-scale geoid undulations have been reported. Consequently, they are of particular interest to test the characteristics and robustness of these long-wavelengths geoid undulations.

Here, we revisit the question of the existence and characteristics of the long wavelengths geoid undulations in the light of the new GRACE satellite gravity data by applying a dedicated analysis technique in spherical geometry: a directional wavelet transform with Poisson multipole wavelets (Hayn & Holschneider 2009). This method allows one to analyze the gravity field in two dimensions on the sphere. The 2-D analysis helps to avoid any possible artifacts due to 1-D along-track filtering. Because they are well localized in space and frequency, the wavelets highlight the directional features in the gravity field at different scales and in different locations. Thus, this goes beyond a spherical Fourier-type analysis as carried out by Wessel *et al.* (1994), providing localized spectra and showing how the dominant scale changes for one area to another. Isotropic multi-scale analysis of the Earth's geoid has been applied by Cadio *et al.* (2011), showing the geoid signature of deep mantle convective upwellings. Directional wavelets on the sphere have been applied by Audet (2011), who jointly analyzed the gravity and topography of the Earth, Venus, Mars and Moon, in order to study and compare the lithospheric structures of these planets.

We first describe our method and how we apply it to the gravity and bathymetry data. We then discuss the significance of the inferred directional patterns by comparison with reference noise models. We validate the method on synthetic directional signals, and finally confirm the existence of large-scale undulations of the geoid, some of them correlated with bathymetry, discuss their characteristics and give some hints to their possible origins.

2 DATA USED

2.1 Gravity

We analyze a set of geoid models based on data from the GRACE satellite gravity mission. These models are provided in the form of spherical harmonics expansions of the geopotential. Some of them are calculated by least-squares adjustment of GRACE measurements only, whereas others also include surface gravity measurements and satellite altimetry-derived gravity. In these combined models, the spherical harmonics up to degree/order 100 (resolution 200 km) are constrained from the GRACE data only, whereas the harmonics of degree/order above 100 are constrained from the surface gravity and satellite altimetry-derived gravity. This reflects the fact that the GRACE measurements are more precise than the surface and altimetric measurements at the lower resolutions, and thus particularly suitable for geoid undulation studies.

To test the robustness of the directional features in the geoid, we analyze the following geoid models:

(1) GRACE-only models: the GGM03S model (Tapley *et al.* 2007) and the EIGEN-GL04S (Biancale *et al.* 2010), complete up to degree/order 180 and 150, respectively, corresponding to a resolution of 110 and 125 km, respectively, and

(2) combined models: the GGM03C model (Tapley *et al.* 2007) and the EIGEN-GL04C model (Foerste *et al.* 2008), complete up to degree/order 360 (resolution 55 km) and the EGM2008 model (Pavlis & Holmes 2004; Pavlis *et al.* 2008), complete up to degree/order 2160 (resolution 9 km).

Spatial grids of geoid heights are built from these models truncated at degree/order 100 for the GRACE-only models and 360 for all the combined models. The grids step is $0.5^\circ \times 0.5^\circ$. Fig. 1 (top panel) shows the gravity anomaly maps calculated from the EGM2008 model.

Satellite-based models may exhibit directional artifacts with shapes following the satellite tracks. In the case of the GRACE data, these patterns are known as 'stripes', and they are elongated in the north-south direction (Chen *et al.* 2005; Swenson & Wahr 2006). To make sure that the observed directional patterns in the geoid are not such artifacts, we apply significance tests using *a priori* noise models (see Section 4) and also compare them to a bathymetry data set.

2.2 Bathymetry

We also search if the directional structures in the geoid have a bathymetric expression. Here, we analyze the General Bathymetric Chart of the Oceans (GEBCO) 1 min grid (Gebco 2003). Fig. 1 (bottom panel) shows the world oceans bathymetry with the main tectonic structures. This bathymetric map is based on a compilation of ship depth soundings, interpolated between the ship tracks. The grid quality thus degrades in areas where ship soundings are sparse,

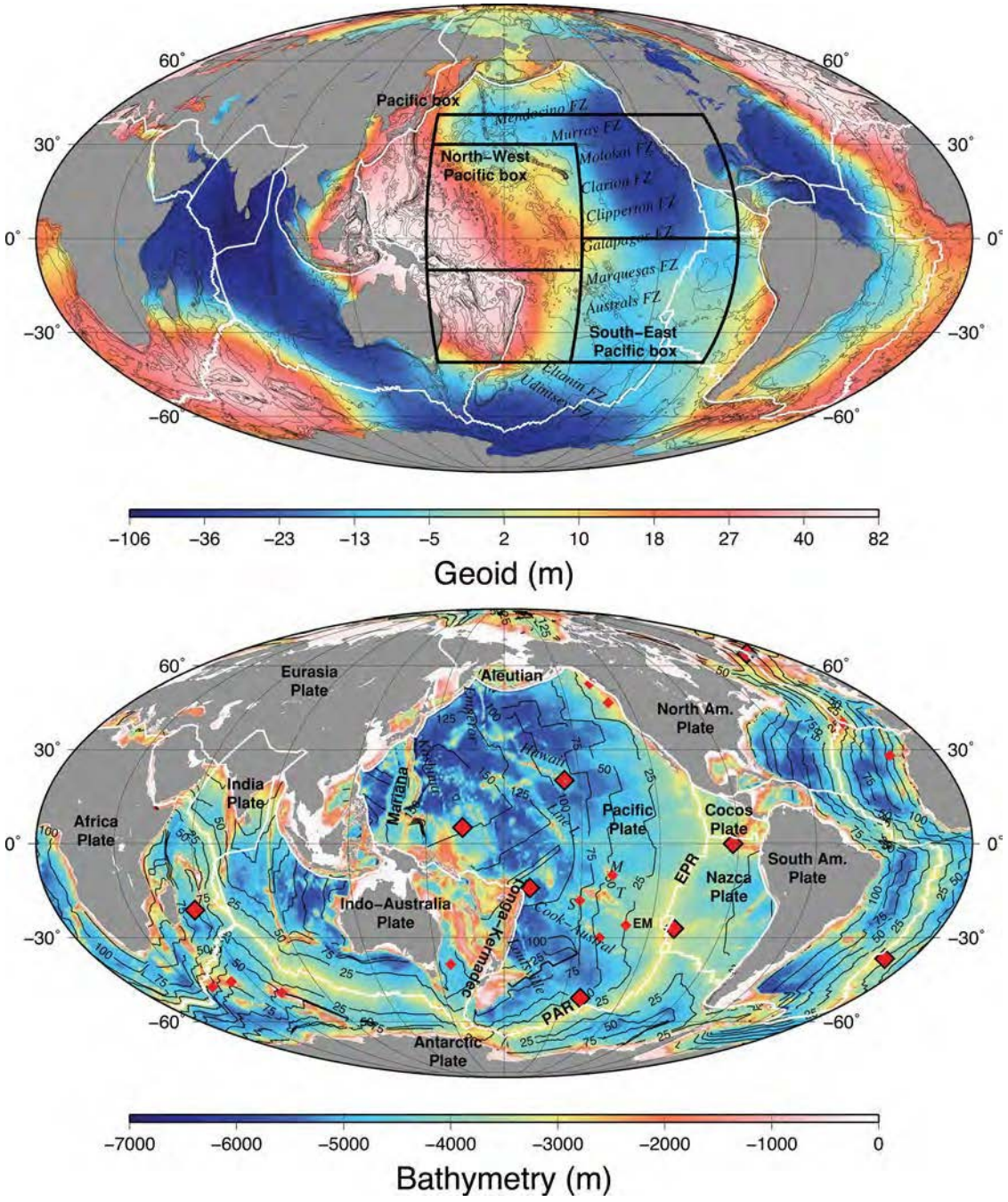

Figure 1. Top Panel: Map of the geoid anomalies of the world oceans computed from the EGM2008 model Pavlis *et al.* (2008) up to degree/order 360. The 1000 m contours of the GEBCO bathymetry are superimposed in black lines. The fracture zones of the Pacific ocean are indicated. The following abbreviations have been used: FZ: fracture zone, EM: easter microplate. The three areas (Pacific box, North–West Pacific box and South–East Pacific box) where the scaling properties of the geoid undulations are studied in Fig. 22 are delimited by red boxes. Bottom Panel: Map of the GEBCO bathymetry of the world oceans, with the tectonic plates limits and the major islands chains of the Pacific. The 25, 50, 75, 125, 150 and 175 M.y. isochrons of the ocean floor from Müller *et al.* (1997) are superimposed in black lines. Tectonic plate boundaries are indicated in white lines. Major and secondary hotspots are indicated in resp. large and small red diamonds. The following abbreviations have been used: EPR: East Pacific Rise, PAR: Pacific-Antarctic Ridge, EM: easter microplate, M: Marquesas islands, T: Tuamotu islands, S: society islands.

but the advantage is that the version of the GEBCO grid that we use is fully independent from satellite altimetry-derived gravity, and that its error pattern differs from errors related to the track spacing of satellite data. Thus, in addition to providing hints on the geodynamic origin of the observed geoid anomalies and separating superficial contributions from deeper ones, the bathymetric data also let us assess the robustness of the observed features.

3 DIRECTIONAL CONTINUOUS WAVELET ANALYSIS

3.1 Principle

Wavelet analysis is a tool for location-frequency analysis (Holschneider 1996). To highlight directional structures at different

scales in the geoid, we apply a continuous wavelet analysis using directional wavelets. Let us denote $\{\psi_a\}_{a>0}$ the family of used wavelets. These are the analysing functions of scales defined by the scale parameter, $a > 0$. They represent the local directional features we search for in the data. The scale of the wavelet corresponds to the size of the feature and to the wavelet width. The wavelet ψ_a can be translated to the position of interest, given by the latitude and longitude (ϑ, φ). Wavelet analysis on 2-D signals, such as signals on the sphere, can be done by means of isotropic wavelets, which are fully defined by their scale and position, or by means of anisotropic, directional, wavelets. For directional wavelets, an additional parameter is required to define the wavelet azimuth $0^\circ \leq \alpha \leq 170^\circ$. We thus work with a four parameter family of wavelet functions:

$$\psi_{a,\alpha,\vartheta,\varphi} = \mathcal{R}(\alpha)\mathcal{T}(\vartheta, \varphi)\psi_a.$$

$\mathcal{T}$ is the operator which translates the wavelet to the position given by latitude ϑ and longitude φ. $\mathcal{R}$ is the operator which rotates the directional wavelet to the required azimuth. Its application to the wavelet ψ_a is defined as

$$\mathcal{R}(\alpha)\mathcal{T}(\vartheta, \varphi)\psi_a(\boldsymbol{x}) = \psi_a(R_z^{-1}(\vartheta)R_y^{-1}(\varphi)R_z^{-1}(\alpha)\boldsymbol{x})$$

where $R_y(\vartheta)$, $R_z(\vartheta)$ rotate vectors around the angle ϑ, the y- or z-axis being the rotation axis respectively.

Since the investigated scales, positions and azimuths continuously vary, this analysis is called a Continuous Wavelet Transform (hereafter referred to as CWT). In practice, the scales, positions and azimuths are finely and regularly sampled, so that no big gaps arise in the investigated range of scales and positions.

Using directional wavelets, we analyze the presence of local features of different scales a, orientations α and positions (ϑ, φ) in a signal s by calculating its wavelet transform as follows:

$$\mathcal{W}_{\{\psi_a\}}s(a, \alpha, \vartheta, \varphi) = \langle \psi_{a,\alpha,\vartheta,\varphi} | s \rangle,$$

where $\langle f | g \rangle$ is the scalar product of two functions f and g defined on the sphere.

3.2 Directional Poisson wavelets

The wavelets we choose for our analysis are the directional Poisson wavelets presented in Hayn & Holschneider (2009). They are defined by taking derivatives of the Poisson kernel of potential fields, which makes them very suitable for potential fields analysis. In contrast to the isotropic Poisson wavelets (Iglewska & Holschneider 2007), constructed by radial derivations of the Poisson kernel—see Chambodut *et al.* (2005) for an example of application to potential fields modelling—we build directional wavelets by taking derivatives ∂_ξ of the operations $\mathcal{T}_{\hat{\boldsymbol{e}}_z}(\xi, 0)$ that are used for translating the wavelet on the sphere to the latitude ξ:

$$\psi_a^n(\hat{\boldsymbol{x}}) = \partial_\xi^n \mathcal{T}_{\hat{\boldsymbol{e}}_z}(\xi, 0) a^n \sum_l e^{-al} Q_l(\hat{\boldsymbol{x}} \cdot \hat{\boldsymbol{e}}_z). \quad (1)$$

The function Q_l is defined as: $Q_l = (2l + 1)P_l$, where P_l is the Legendre polynomial of degree l. Bold letters marked with a hat stand for vectors of unit length. The order n of the directional Poisson wavelets regulates the directional filtering during the wavelet analysis by changing the ratio between the wavelet width and length. Increasing order increases the directional selectivity of the wavelet, as shown in Fig. 2. The angular resolution Δ angle behaves like

$$\Delta\text{angle} \simeq \frac{1}{\sqrt{n}}.$$

The non-dimensioned scale parameters a correspond to spatial scales of $a \cdot 20000/n$ km.

Lastly, the directional Poisson wavelet transform of a potential can be calculated directly from the sources of the potential anomalies, by means of multipolar weighting functions, as explained in what follows and in the appendices.

3.3 Analysis of the geoid and link to density distribution

In a similar way as in Panet *et al.* (2006), the CWT $\mathcal{W}_{\{\psi_a^n\}}\Phi(a, \alpha, \vartheta, \varphi)$ of the gravity potential Φ using directional Poisson wavelets ψ_a^n can be written as an integral of the densities $\delta\rho$ over the Earth's volume V_E, involving a weighting function that goes deeper inside the Earth as the scale increases:

$$\mathcal{W}_{\{\psi_a^n\}}\Phi(a, \alpha, \vartheta, \varphi) = G \int_{V_E} d^3\boldsymbol{x}\ \delta\rho(\boldsymbol{x})\mathcal{R}(\alpha)\mathcal{T}(\vartheta, \varphi)F_a^n(\boldsymbol{x})$$

where the densities are weighted with the multipole weighting function:

$$F_a^n(\boldsymbol{x}) = \partial_\xi^n \mathcal{T}_{\hat{\boldsymbol{e}}_z}(\xi, 0) a^n e^a \frac{1}{\left|\boldsymbol{x} - R_E e^a \hat{\boldsymbol{e}}_z\right|}.$$

As the geoid is simply related to the potential in the spherical approximation, a similar expression also holds for the CWT of the geoid. In contrast to the case of isotropic wavelets, for which the shape of the weighting function is isotropic, we now have directional weighting functions, as represented in Fig. 2. The derivation of this result is presented in Appendix A.

3.4 Analysis of the geoid effect of the bathymetry

The part of the gravity potential Φ that is associated with the bathymetry shall be denoted by $\Delta\Phi$. We calculate the CWT of $\Delta\Phi$ following the approach described in Panet *et al.* (2006). The CWT can be written again as the integral of the bathymetric load $\Delta\sigma$, weighted with a multipolar function F_a^n centered at the analysis point (ϑ, φ) and rotated to azimuth α:

$$\mathcal{W}_{\{\psi_a^n\}}\Delta\Phi(a, \alpha, \vartheta, \varphi) = G R_E \left\langle \Delta\sigma \left| \mathcal{R}(\alpha)\mathcal{T}(\vartheta, \varphi)F_a^n \right\rangle\right.$$

with the weighting function given by:

$$F_a^n(\hat{\boldsymbol{x}}) = \partial_\xi^n \mathcal{T}_{\hat{\boldsymbol{e}}_z}(\xi, 0) a^n e^a \frac{1}{|\hat{\boldsymbol{x}} - e^a \hat{\boldsymbol{e}}_z|}.$$

The derivation of these expressions is presented in Appendix B.

3.5 Scale and orientation of directional structures

We now explain how the CWT can be used to infer the characteristic scale and direction of an anisotropic geophysical structure.

3.5.1 Determination of dominant directions

The observed gravity field results from the superimposition of different contributions, corresponding to various geodynamic processes. Each process is associated with a local geoid anomaly, which produces in the wavelet domain a coherent pattern of CWT coefficients in the correponding area, with a maximum of energy of the coefficients around its characteristic scale a and orientation α (if it is non-isotropic).

For each fixed position $\hat{\boldsymbol{x}}$ and scale a, the wavelet transform is a function $f_{\hat{x},a}(\alpha)$ only depending on direction. We define the

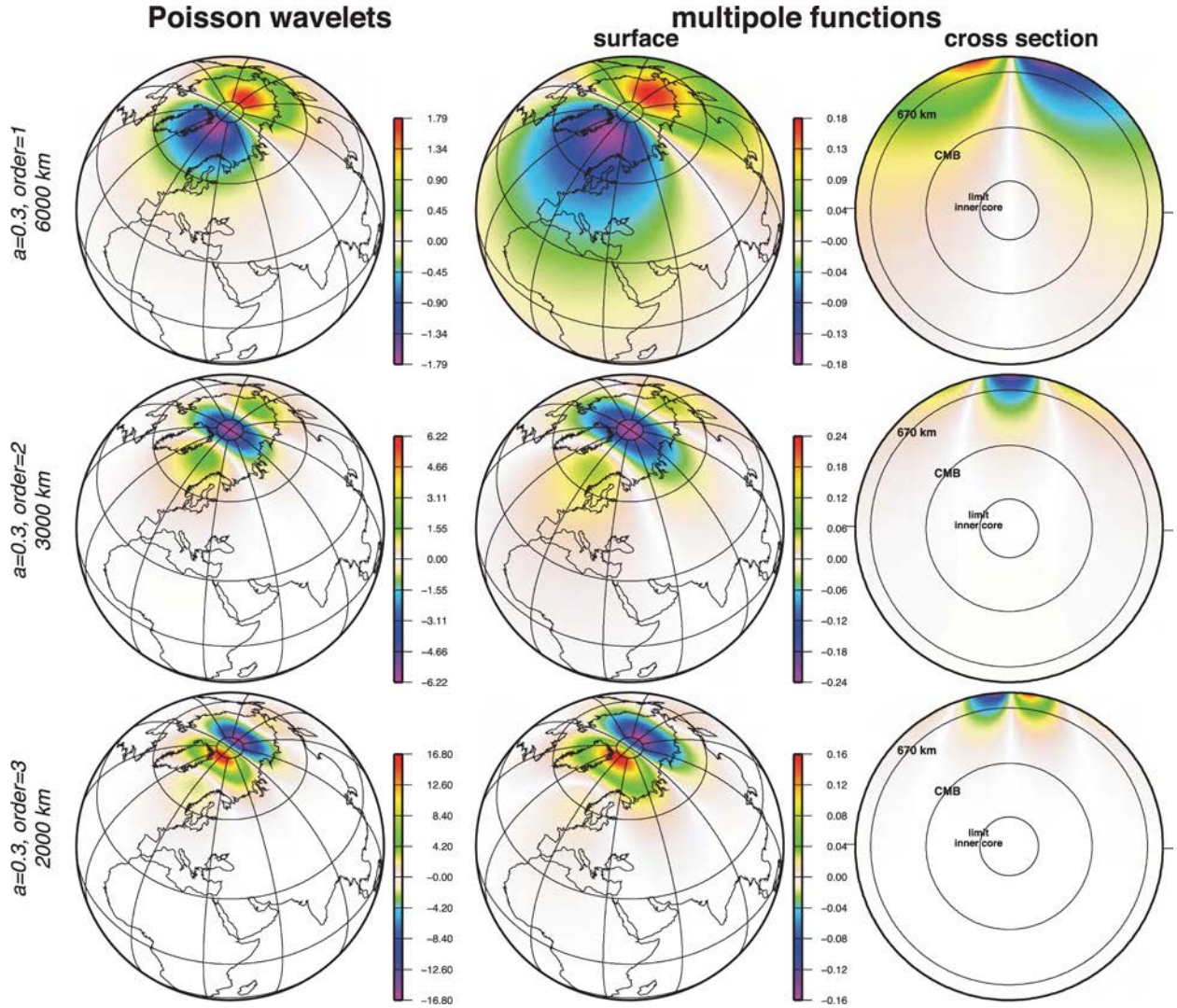

Figure 2. Maps of directional Poisson wavelet functions (left column). Maps (middle column) and cross-sections (right column) of the associated multipole weighting functions of densities. Each line corresponds to a different order of the wavelets: order 1 (top line), order 2 (middle line) and order 3 (bottom line). The wavelet scales are 6000 km for order 1, 3000 km for order 2 and 2000 km for order 3.

Table 1. Average intervals of influence/km.

Scale d_0 (km)	200	300	600	800	1000	...	1600
Interval of influence (km)	140–270	220–400	430–800	580–1070	720–1340	...	1160–2150

dominant direction at this position and scale as the direction α for which $f_{\hat{x},a}$ is maximum in absolute value, and represent the observed α on a series of maps at different scales.

3.5.2 Signature of a signal of characteristic scale in the CWT

The characteristic scales in the CWT are well represented in the wavelet spectra, that is the energy of the wavelet coefficients corresponding to the different scales a. Because the wavelets are non-orthogonal, a peak in the wavelet spectrum always spreads over an interval of scales centered around its maximum.

Regarding the ideal case of an analyzed signal with a spherical harmonics spectrum only consisting of contributions of degree ℓ_0, which corresponds on the Earth with a circumference of approximately 40 000 km to the spatial resolution of $d_0 = \frac{20000}{\ell_0}$ km, the wavelet spectrum behaves like $(a\ell_0)^{2n}e^{-2a\ell_0}$. It becomes maximal for the corresponding non-dimensioned scale parameter $\hat{a} = \frac{n}{\ell_0}$ and spreads over an interval of influence of scale d_0, given in Table 1. It shows for instance that a peak at the scale corresponding to $d_0 =$ 300 km in the wavelet coefficients spreads over the adjacent wavelet coefficients with wavelength 200–400 km.

3.5.3 Local relative wavelet spectra

Local wavelet spectra are defined as the square root of the mean squared wavelet coefficients, averaged over a local area around the point (θ, ϕ), separately for each scale and for directions selected according to the kind of spectrum: for 'dominant direction spectra', the CWT coefficients for the dominant direction are selected, and for 'fixed direction spectra' the CWT coefficients for a chosen

azimuth are selected. As shown in the following, the latter is more appropriate to highlight a local directional pattern.

When one looks for a local anisotropic signal of small amplitude in a wide area, the obtained local maximum in the wavelet spectra of this single signal can be quite small as compared to the variability of the global spectrum. This is the case when we investigate geoid undulations of small amplitudes over an entire ocean. According to Kaulas rule, a decrease of the average gravity field spectra dominates. To enhance small undulations, we thus normalize the wavelet spectrum by the wavelet spectrum of the background and obtain a 'relative spectrum'. The background value is obtained by averaging the absolute values of the CWT coefficients at each scale over all the orientations and over the whole oceanic domain. The obtained relative spectrum thus represents the local deviation to the average behaviour, enhancing small local structures in the geoid. Because of the applied normalization, a scaling factor (typically, between 1.2 and 2) needs to be applied to the wavelet scale in order to derive the undulation scales, as described in Appendix C. The obtained scales are called 'analysis scales' in the remainder of this paper. The scaling factor has been taken into account in all the maps and spectra of this paper.

4 SIGNIFICANCE OF THE CWT

Before interpreting the maps of dominant directions, and using the corresponding CWT coefficients for determining dominant scales, one must check that the dominance of a direction in the geoid is clear enough. In this section, we explain how we test whether the dominant directions are significant and thus how we discard areas where no clear direction dominates.

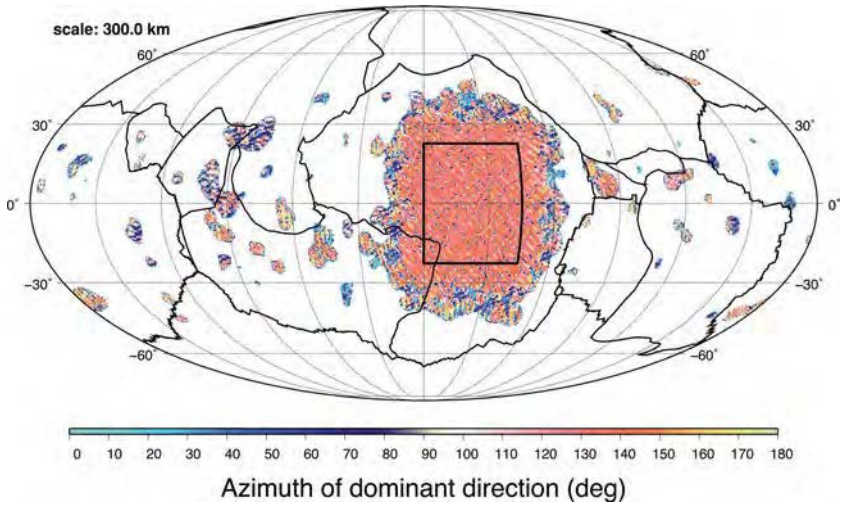

Figure 3. Map of dominant directions of the 300 km scale wavelet transform of a synthetic undulation with azimuth 45° and scale 300 km, superposed to Gaussian white noise. The noise-to-signal amplitude ratios is 1:1. Entropy and amplitude masks are applied. The black rectangle marks the area of the signal.

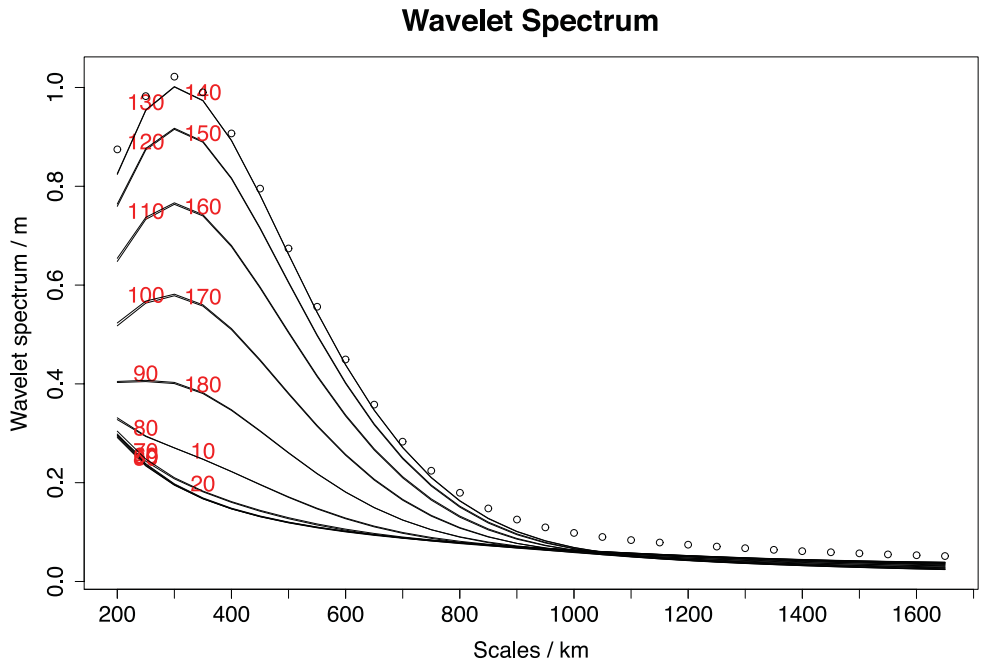

Figure 4. Directional wavelet spectra (in black solid lines) of a 300 km scale synthetic undulation superposed to Gaussian white noise, for each investigated direction (noted in red). The spectrum for the dominant directions is given in circles. The noise-to-signal amplitude ratio is 1:1.

4.1 Threshold on the entropy

To quantify the dominance of a direction at a position $\hat{\boldsymbol{x}}$ and scale a in the geoid, we use the entropy of the directional distribution of its CWT coefficients at this position and scale. The entropy is a common measure of disorder, as described in Landsberg (1984). It becomes maximal for a totally disordered system, that is a system whose states all occur with the same probability. Here, we consider the system of all wavelet transform coefficients $\{c(a, \alpha_i, \hat{\boldsymbol{x}})\}_{i=1,\ldots,18}$, at scale a and averaged over an area centred at position $\hat{\boldsymbol{x}}$, which

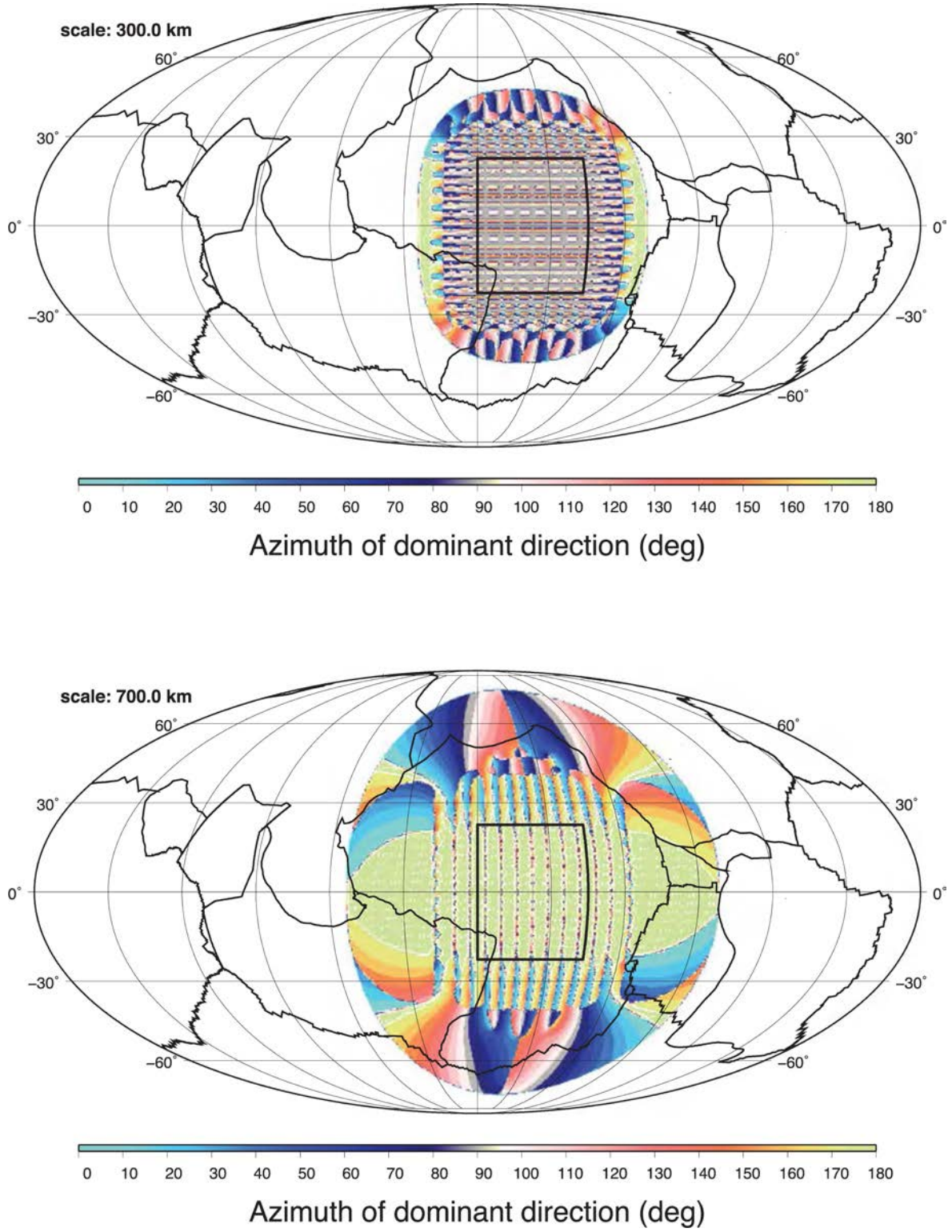

Figure 5. Maps of dominant directions of the 300 km (top panel) and 700 km (bottom panel) scale wavelet transform of a superposition of two synthetic undulations of directions 0° and 90° azimuths and scales 300 and 700 km. The ratio between the amplitudes of the two undulations is 1:1. The black rectangle marks the area of the signal.

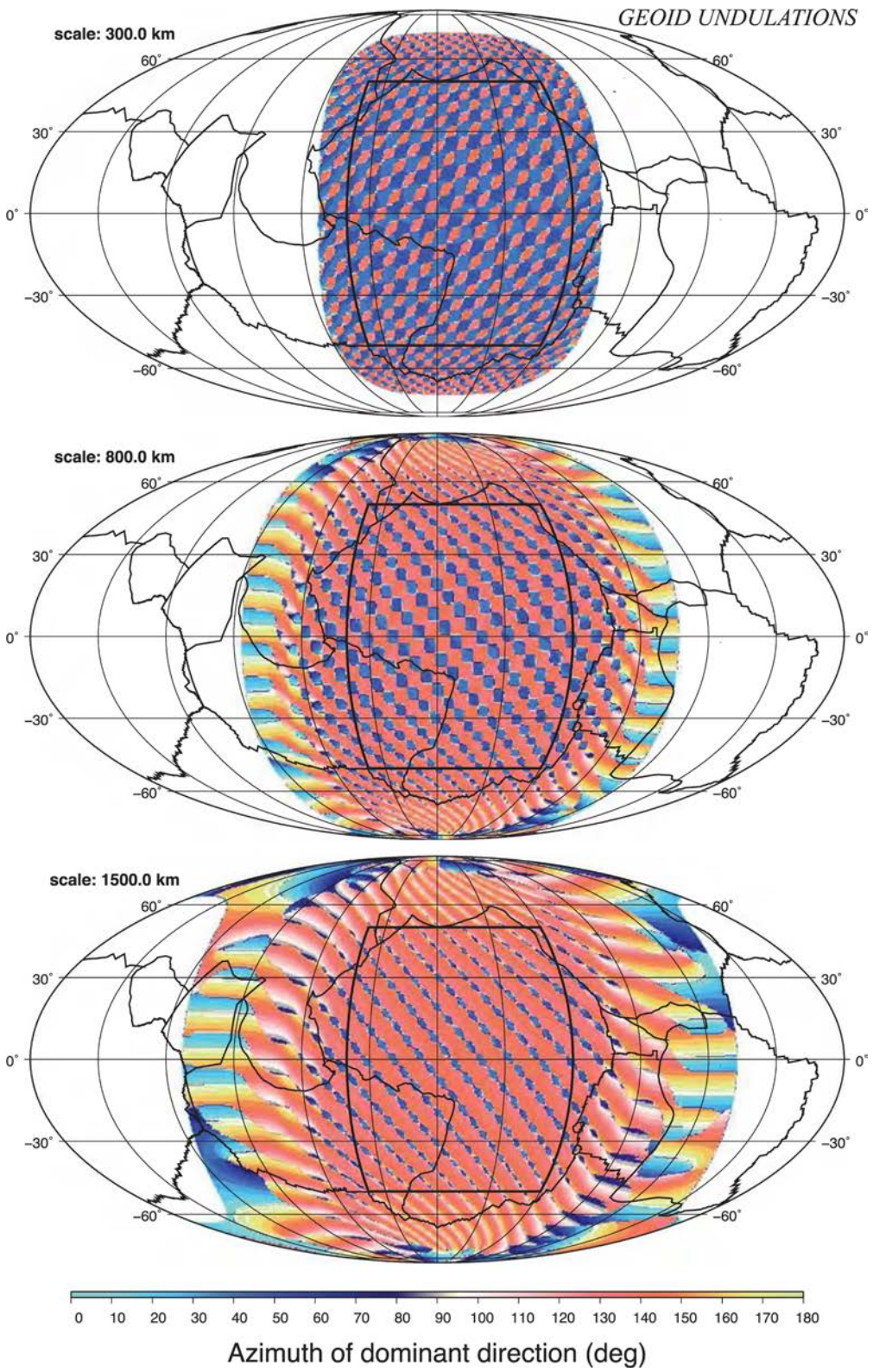

Figure 6. Maps of dominant directions of the 300 km (top panel), 800 km (middle panel) and 1500 km (bottom panel) scale wavelet transform of a superposition of two synthetic undulations of directions 0° and 90° azimuth and scales 800 and 1000 km. The ratios between the amplitudes of the two undulations is 8:10. Note how the dominant direction and associated spatial pattern changes as the scale increases. The black rectangle marks the area of the signals.

only depends on the orientation α. For a distribution over azimuths $\alpha_1 = 0^\circ, \alpha_2 = 10^\circ, \ldots, \alpha_{18} = 170^\circ$, the entropy is calculated via:

$$S(a, \hat{\mathbf{x}}) = -\sum_i \frac{c(a, \alpha_i, \hat{\mathbf{x}})^2}{\|\boldsymbol{c}(a, \hat{\mathbf{x}})\|^2} \log \frac{c(a, \alpha_i, \hat{\mathbf{x}})^2}{\|\boldsymbol{c}(a, \hat{\mathbf{x}})\|^2}$$

with $\|\boldsymbol{c}(a, \hat{\mathbf{x}})\|^2 = \sum_j c(a, \alpha_j, \hat{\mathbf{x}})^2$.

A dominant direction in the CWT of the geoid is considered significant if the entropy of the distribution of the CWT coefficients over the azimuths, at the investigated location and scale, is low enough, meaning that all directions are not equally probable. To define a threshold below which entropies are said to indicate 'significantly' oriented structures, we use a white noise model, where no oriented structures are expected, as a reference. For each scale a, we calculate a histogram of the entropy values of the directional distributions of the CWT of the white noise model at the different locations, and the threshold T_a for the scale a is set to the entropy value lower than 90 per cent of all entropy values at this scale. Then, with a confidence level of 90 per cent, we consider a dominant direction in the geoid at scale a to be significant if the entropy of the directional distribution of the geoid CWT coefficients at this location is lower than T_a.

4.2 Threshold on the amplitude

Apart from using entropy for the determination of areas where a directional structure is present in the geoid, in a second test we check that the CWT is significant with respect to the amplitude. For the application on the gravity field and the bathymetry, the precision thresholds at each scale T_a are determined from the wavelet transform of the white noise signal with a standard deviation of 20 cm, corresponding to the estimated average differences between the geoids from the spherical harmonics models described in Section 2.1. Using histograms of the values of the CWT coefficients of the noise model, the precision thresholds T_a are chosen such that they lead to a 90 per cent confidence estimate.

However, for the gravity field and the bathymetry, we observed that all areas that are inferred significant with respect to the entropy, are also significant with respect to the amplitude. Only when considering higher amplitude thresholds, the amplitude masks become effective (see end of Section 6.1.3 and Fig. S2 in the Supporting Information). In this work, the amplitude masks are mainly applied for emphasizing important areas at the synthetic tests (Section 5).

5 VALIDATION OF THE METHOD

To validate our directional analysis method, we first apply it on a series of synthetic signals. By analyzing regular and irregular synthetic undulations with different amplitudes and noise levels, we demonstrate that we are able to recover their characteristic directions and scales without generating artifacts.

5.1 Generation of the synthetic undulations

We build local synthetic undulation signals with a fixed orientation by rotating a loxodrome around the Earth's pole axis. The signal amplitude along this loxodrome is the sine of the rotation angle. The period of the sine determines the scale of the signal. The loxodrome azimuth determines the direction of the signal.

5.2 Test 1: one undulation with noise

We first analyze synthetic undulations of amplitude equal to 1 and wavelength 300 km degraded by a white noise with standard deviation of 0.1, 0.5 and 1.0.

The direction of the loxodrome clearly appears on all maps up to 700 km scale for the highest noise level, 800 km scale at the middle noise level, and 1100 km scale for the lowest noise level. Fig. 3 shows the dominant directions at 300 km for the highest noise level

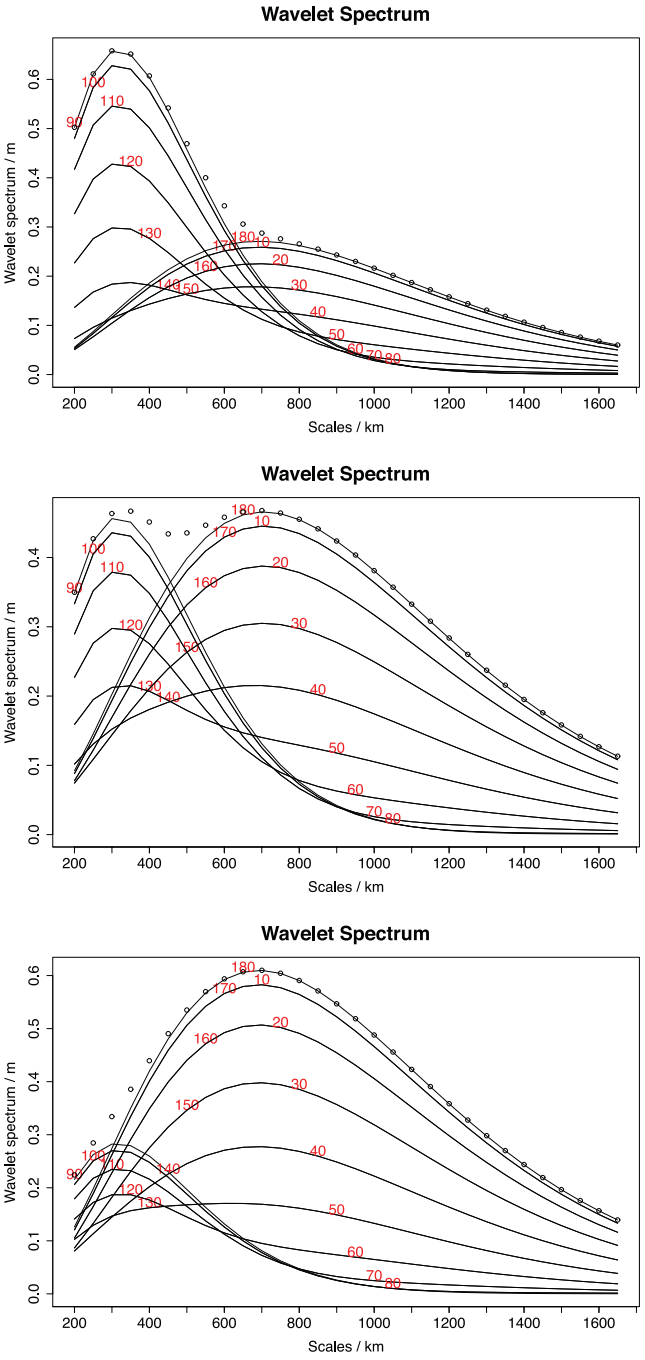

Figure 7. Directional wavelet spectra (in black solid lines) for the superposition of two synthetic signals of of directions 0° and 90° azimuths and scales 300 and 700, for each investigated direction (noted in red). The spectrum for the dominant directions is given in circles. The amplitudes ratio of the two signals are a_{300}: a_{700} = 12.5:4.5 (top panel), 1:1 (middle panel), 5:12 (bottom panel).

(amplitude 1). As previously described, entropy and amplitude masks are applied on this map. The loxodrome direction is observed more or less uniformly over the whole area covered with this signal. With increasing difference between the analysis scale and the scale of the signal, the white noise degradation of the loxodromes signature progressively appears in the maps of dominant directions. This degradation is observed in the areas where the CWT amplitude of the loxodrome is close to zero, because the direction is never well determined in these areas and the influence of the noise is larger there. This is the reason why the patterns of constant direction in the map of dominant directions (orange lines) show a structure related to the loxodrome scale at all analysis scales. Fig. 4 shows the local wavelet spectra for each investigated direction (in red on the plots), for the highest noise level. In this test, the scaling factor is equal to 1. We clearly observe a maximum at 300 km scale, corresponding to the loxodrom wavelength. Moreover, the amplitude of the peak increases when the wavelet direction gets closer to that of the signal. When the amplitude vanishes, no dominant direction is evidenced, as expected.

5.3 Test 2: two undulations without noise

We now address a more complex case, to separate superposed undulations of different scales. For a better comprehension of the effect of this superposition, we do not add noise. In a first series of tests, we consider undulations of wavelengths 300 and 700 km. We test numerous combinations of amplitude ratios and directions. Fig. 5 shows the obtained maps of dominant directions for scales 300 and 700 km, in an example where the amplitude ratio between undulations is 1:1 and their azimuths are 0° and 90°, respectively. The dominant direction obtained for the total synthetic signal changes from the first azimuth to the second at a scale that depends on the ratio of the undulation amplitudes. For an amplitude ratio of about a_{300}: a_{700} = 1:3, the 700 km scale undulation dominates over the 300 km scale undulation in all maps of dominant directions for scales larger than 200 km. On the contrary, for an amplitude ratio of about a_{300}: a_{700} = 3:1, the 300 km scale undulation dominates over the 700 km scale undulation in the maps of dominant directions for scales up to 700 km. At each scale, exclusively the two directions of the superposed undulations appear on the direction map, whereby one of both dominates according to the descriptions above. This is illustrated on the maps of dominant directions of Fig. 6, which corresponds to a superposition of a 800 km scale loxodrome, with azimuth 50°N, and a 1000 km scale loxodrome, with azimuth 140°N. The amplitude ratio is 8:10.

Let us now discuss the wavelet spectra. They are shown in Fig. 7 in the case of the 300/700 km loxodromes superposition, with respective amplitude ratios of a_{300}: a_{700} = 12.5:4.5, 1:1 and 5:12, and azimuths 0° and 90°. We find two peaks at the undulations scales in the fixed direction spectra, with maximum energy for the direction of the undulation, and with a progressive transition from one dominant scale to the other, when the investigated direction varies. On these figures, we also represent with circle markers the wavelet spectrum for the dominant direction observed at each scale. It has two maxima for undulations of similar amplitudes, but when the difference in undulations amplitude increases, the global maximum—still at the scale of the main undulation—progressively hides the second local maximum in this spectrum. This holds for signals with arbitrary differences in the azimuth. On the other hand, the fixed direction spectra clearly separate the two maxima whatever their relative amplitude.

If the synthetic signals look more similar (closer scales or orientation), the fixed direction spectra are still efficient in isolating the two undulations (see Fig. 8). They still allow distinguishing two signals of close scales as soon as their directions differ a little. As an example, Fig. 8 shows the spectrum for a superposition of two loxodromes with scales 500 and 700 km and a direction difference as low as 10°. On the contrary, the peak in the dominant direction spectrum is located inbetween the two undulations scales. Such spectrum makes it possible to give the right scaling of the major undulation only if the scales do not belong to each other's influence interval (see Table 1). The fixed direction spectra are thus more reliable than the dominant direction spectrum to determine the characteristic scales of the synthetic signals.

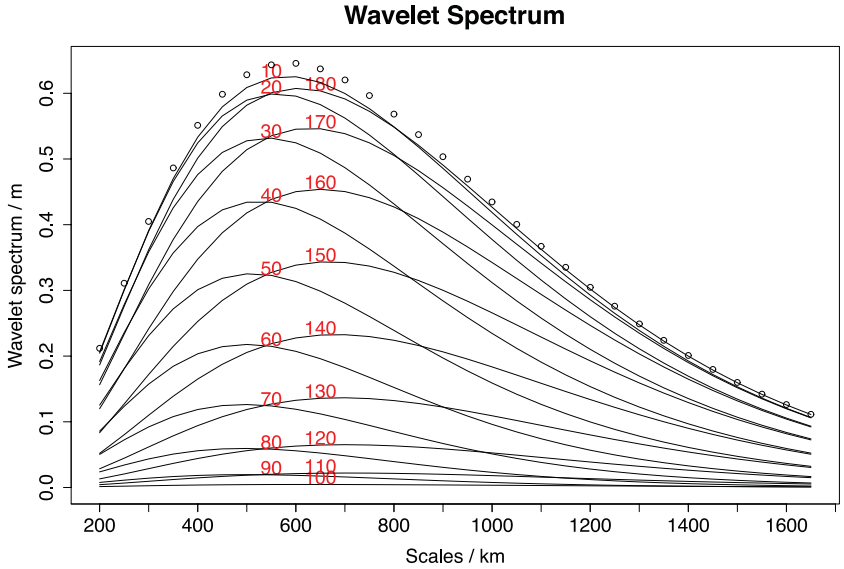

Figure 8. Directional wavelet spectra (in black solid lines) for the superposition of two synthetic signals of close scales (500 and 700 km) and close directions, for each investigated direction (noted in red). The spectrum for the dominant directions is given in circles. The direction difference is 10°.

5.4 Test 3: undulations of non-constant amplitude

As real geoid undulations may not have a constant amplitude, we now investigate the effect of variations in the undulation amplitude on the wavelets transforms. We consider a periodic variability of the amplitude, likely to create the largest changes in the CWT, and investigate if such modulation generates large-scale patterns in maps and spectra. The synthetic signal is now built by stringing together three parallel loxodromes with increasing amplitude, and repeating this basis pattern. Doing so, we create a modulated signal, with a carrier wave of 400 km scale and an envelope wave of 1200 km scale.

Fig. 9 shows the obtained wavelet spectra for a progressive variation of amplitudes (amplitudes ratio of 1:2:3 between the three loxodromes of the basis pattern), and for a steeper one (amplitudes ratio of 1:2:9). These spectra always show a unique peak with maximum at the 400 km scale of the loxodromes. The effect of the variations of undulation amplitude is a slower decay of the peak at large scales, leading to a larger tail, especially for the latter amplitudes ratio. It does not create any large-scale pattern in the wavelet transforms.

5.5 Test 4: alignments of non-directional signals

Here, we test if a directional distribution of small-scale non-directional structures can create large-scale peaks in the wavelet spectra and patterns in the direction maps. For that, we create three lines of local, 400 km wide axisymmetric bumps, with a 1000 km spacing between the bumps along the lines and 1400 km spacing between the lines (Fig. 10). At small scales, the wavelet transform detects each bump as an isolated, non-directional feature. Thus,

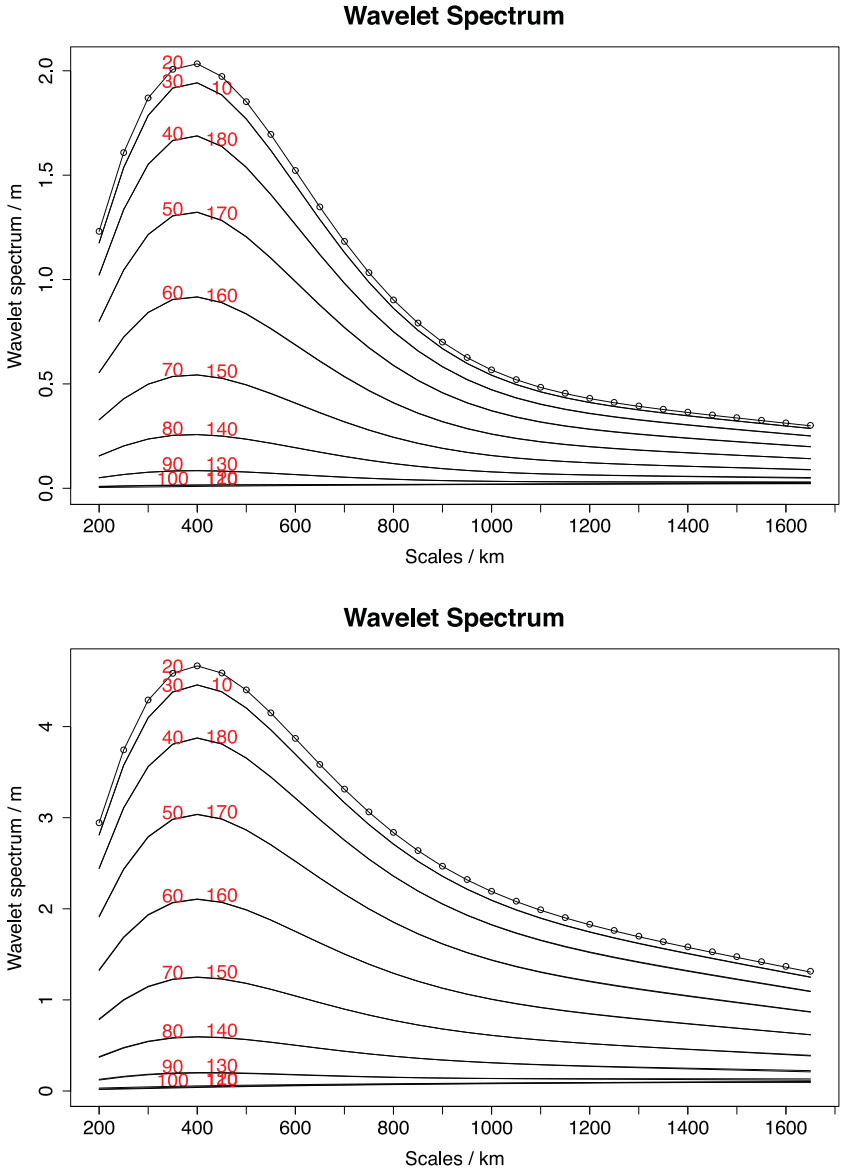

Figure 9. Directional wavelet spectra (in black solid lines) of a synthetic undulation with modulated amplitudes, for each investigated direction (noted in red). The spectrum for the dominant directions is given in circles. The amplitudes ratios of three consecutive oscillations due to the modulation is 1:2:3 (top panel) and 1:2:9 (bottom panel).

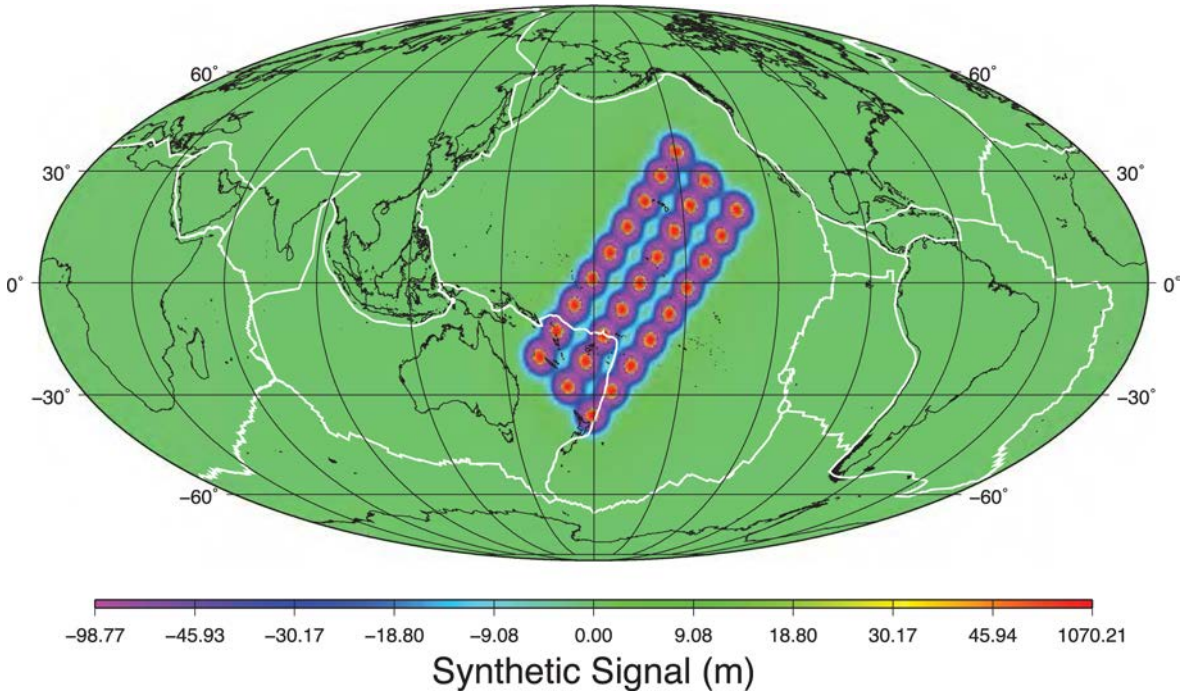

Figure 10. Synthetic signal made of three parallel series of non-directional 400 km scale bumps. The distance between two bumps along the lines is 1000 km, and the distance between two parallel lines is 1400 km.

entropy masks hide the signal at all scales smaller than 700 km on the maps of dominant directions. At larger scales, the coalescence of the bumps in the wavelet transform leads to a directional structure, already visible on Fig. 10. The direction of the bumps alignment is observed in the direction maps at scales larger than 700 km (see Fig. 11), and considered significant according to the entropy masks.

If the elementary bumps were randomly distributed, no directional fabric would appear. Finally, the spectrum of this synthetic signal, based on the points where directions are observed significant, does not show any peak. Indeed, without mask, the spectrum of this signal has a maximum at 400 km scale for all directions, the regular distribution of the bumps only leading to a slower decay and larger

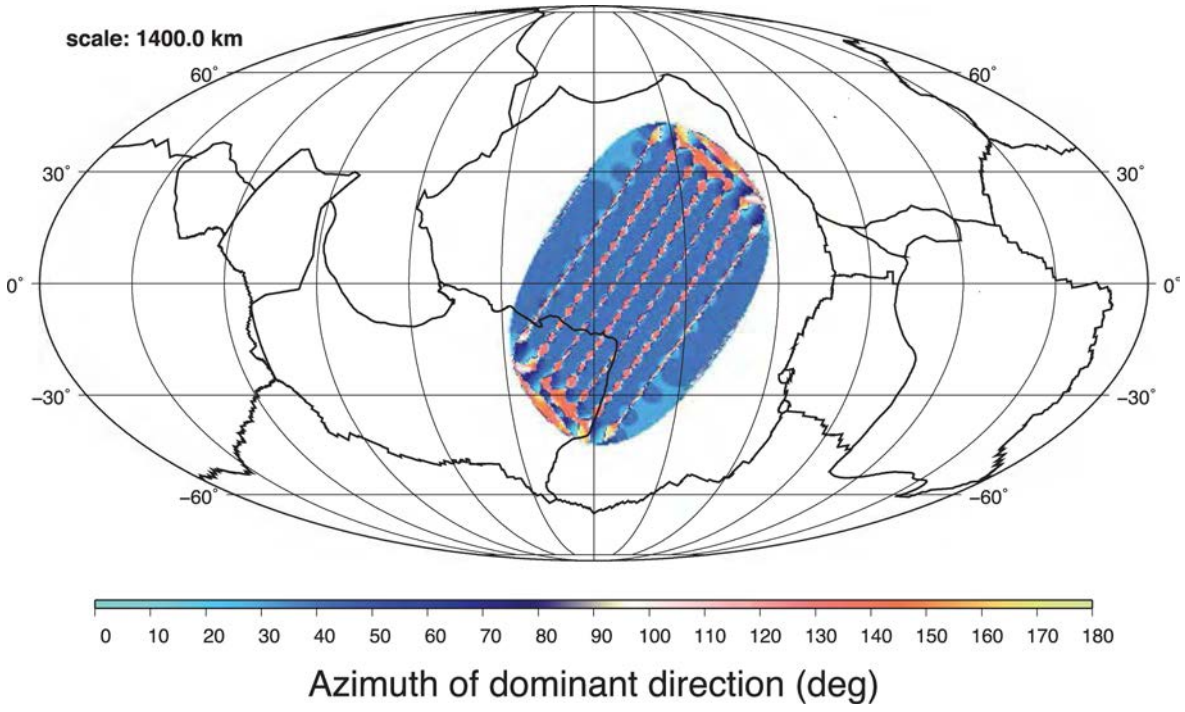

Figure 11. Map of dominant directions of the 1400 km scale wavelet transform of a synthetic signal made of three parallel series of non-directional 400 km scale bumps. At scales smaller than 750 km, the direction maps show no significant direction.

tail at large scales. When taking the masks into account, only the large-scale tail remains, but its amplitude is small and no maximum is observed.

5.6 Undulations superposed to the Earth geoid

We finally superpose a synthetic undulation with 700 km wavelength, 5 m amplitude, and a 90° azimuth, to the EGM2008 geoid. Our aim here is to test the ability of the wavelet transform to pick an undulated pattern among a complex realistic field, and to validate the applied scaling factor. To simulate a realistic scenario, where we cannot separate *a priori* the searched undulation from the background field, the normalization of the spectrum and the associated scaling factor are based on the total spectrum, including EGM2008 and the loxodrome, averaged over all the oceans. For comparison, scaling factors associated with a background field free from the synthetic undulation (EGM2008 only), are also estimated and the corresponding analysis scales are given in red on the spectra.

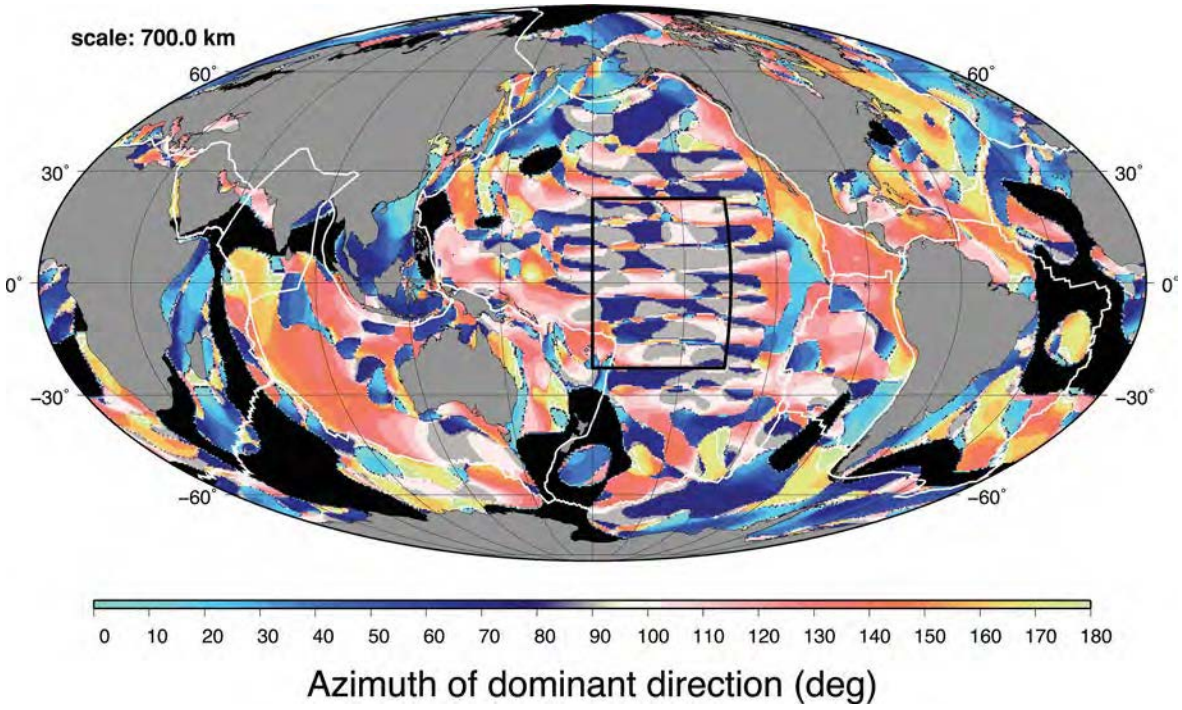

Figure 12. Map of dominant directions of the 700 km scale wavelet transform of a synthetic signal based on the superposition of a 700 km scale synthetic undulation of azimuth 90° and amplitude 5 m to the EGM2008 geoid. The black rectangle marks the area of the synthetic signal.

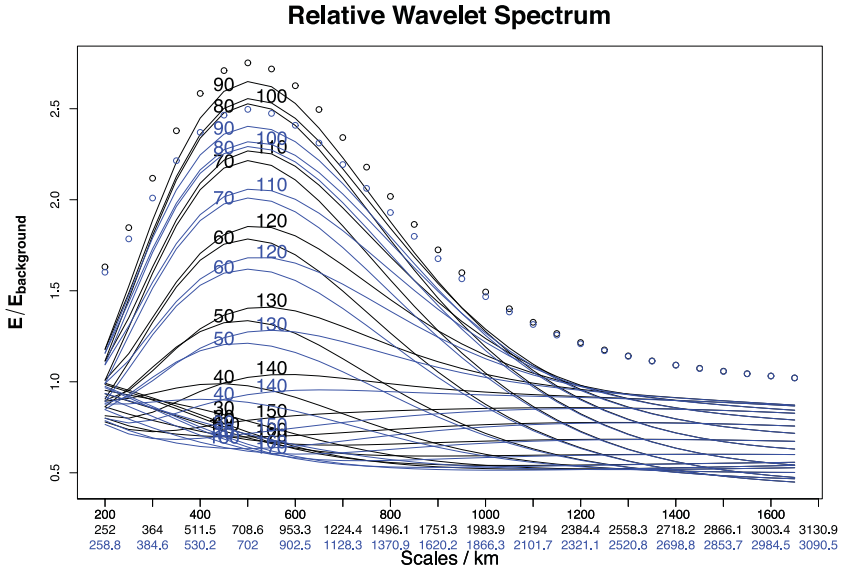

Figure 13. Normalized wavelet spectra for a synthetic signal based on the superposition of a 700 km scale synthetic undulation of 5 m amplitude to the EGM2008 geoid. The spectrum is averaged over the area where the synthetic undulation is localized. Blue solid curves and scale labels correspond to a background spectrum including the searched undulation, black solid curves and lower black scale labels correspond to a background free from the searched undulation, and the upper scale labels correspond to the original wavelet scales. The spectra for the dominant directions are given in circles.

Fig. 12 shows the obtained map of dominant directions at scale 700 km, and Fig. 13 shows the local wavelet spectra, for the case of a 90° oriented undulation of amplitude of 5 m, superposed to the EGM2008 geoid. The undulation direction is detected on the maps (gray lines in the middle of the Pacific), and the spectra show a maximum for an analysis scale close to 700 km, consistent with the undulation wavelength. Moreover, the shape of the spectra and the scale of the undulation are very similar for both ways of computing the background, with or without including the searched undulation. This shows that normalizing the spectra with a background field not perfectly free of some of the searched signals has no significant impact on the scales estimates.

Finally, let us underline that our tests validate the ability of the CWT to retrieve the characteristics of synthetic undulations in terms of scale and direction. They allow us to describe in detail the signature of undulated patterns in the direction maps and spectra. They finally show that peaks in the local wavelet spectra must be interpreted in terms of undulated geoid patterns rather than directional organization of non-directional structures.

6 RESULTS

6.1 Direction and amplitude maps

6.1.1 Parameters and maps

We calculate the directional wavelet transforms of the geoid models and the geoid effect of the bathymetry introduced in Section 3.4 and Appendix B. Wavelet scales vary between 200 km and 1600 km by steps of 50 km (corresponding analysis scales between 280 and 2900 km), and azimuths vary between 0°N and 170°N by steps of 10°. As the different geopotential models lead to very similar results, we restrict to the EGM2008 model in the following.

Figs 14 to 21 show the maps of dominant directions, and the corresponding amplitudes of the wavelet transform, obtained for the EGM2008 geoid and for the GEBCO bathymetry contribution to the geoid, for analysis scales 280, 670, 1450 and 2600 km. In addition, the maps of dominant directions for scales 1050 and 1850 km are shown in Fig. S1 in the Supporting Information. Video Clips

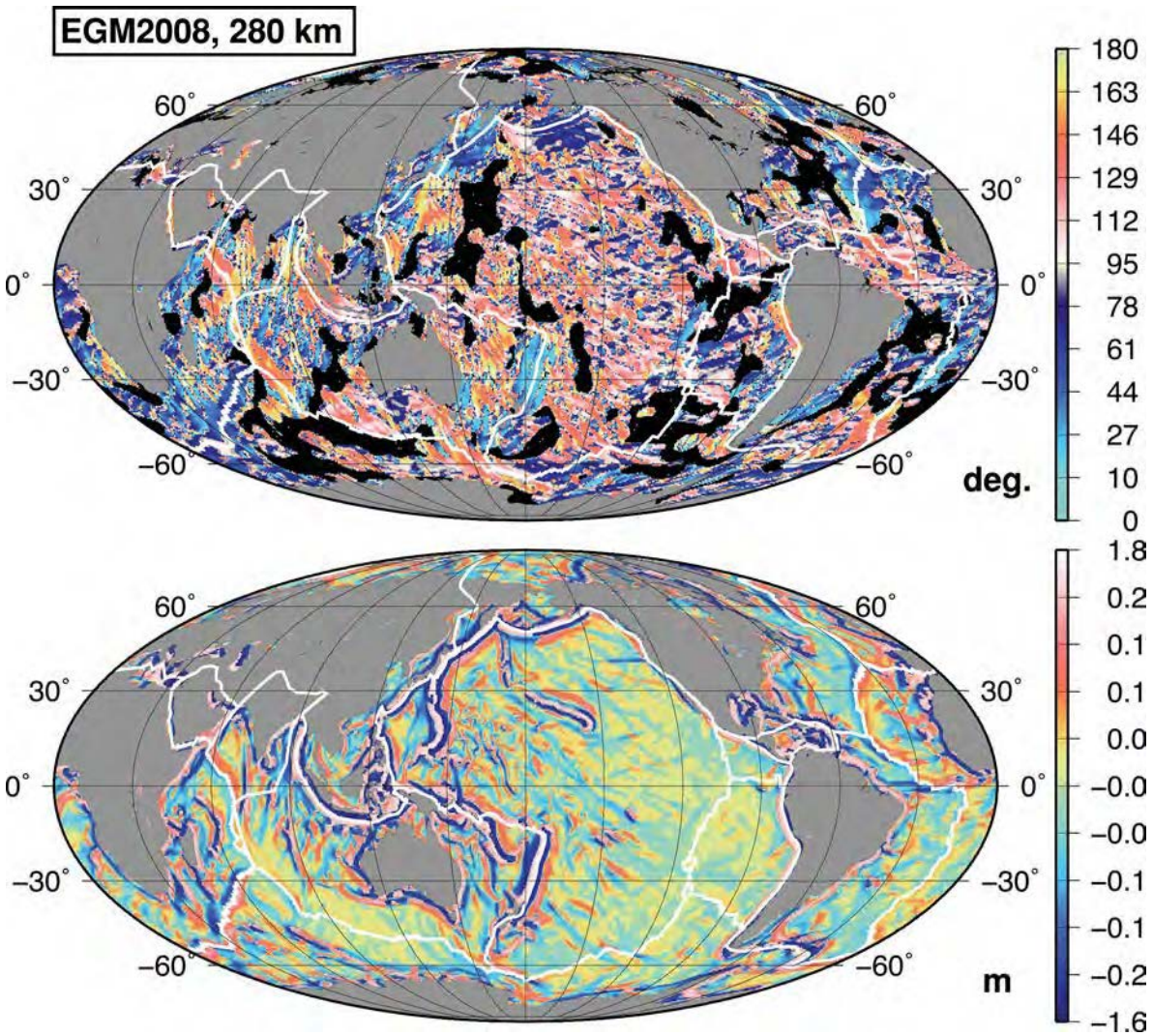

Figure 14. 280 km scale analysis of EGM2008 geoid. Top panel: azimuth of the dominant direction in the wavelet transform; bottom panel: amplitude of the wavelet transform at the dominant direction.

S1 and S2 in the Supporting Information show the maps of dominant directions for all calculated scales, presented as movies. Masks are applied on these maps in areas where no significant dominant direction is observed, as explained in Section 4.

6.1.2 Complementarity of direction and amplitude maps

The maps of dominant directions and of amplitudes are complementary. Whereas the former inform on the presence of directional fabrics in the geoid, the latter inform on the amplitude of these structures. Because of the anti-symmetric shape of the wavelets, an elongated bump—or trough—in the geoid is associated with the succession of a maximum and a minimum in the CWT, with the change of sign at the top (resp. bottom) of the bump (resp. trough). This is illustrated in Figs 14 and 18 (bottom panels), where the signature of subduction zones is associated with two parallel, blue and orange lines. At small scale, the major pattern of the subduction zones and some islands chains such as Hawaii-Emperor dominates in these maps and tends to hide smaller amplitude undulations within the oceans. This is where direction maps are helpful, because they show the small amplitude structures more clearly. As an example, in Fig. 14 (top panel), areas of north–south azimuth can be observed in the Indian Ocean, on the Indo-Australia plate (blue patches). On the Pacific plate, orange patches cover a large part of the plate, indicating NW/SE trending directional structures.

6.1.3 Structure and significance of the directional patterns

The synthetic tests show that, at a given scale, a dominant direction can be observed in an area wider than the considered scale: this means that the whole area is covered with elongated structures at this scale. This is illustrated in Figs 14 or 17 (top panels), where broad areas of the Pacific ocean are associated with a 120° N oriented geoid fabric.

In many of these wide areas, the patches associated with a dominant direction are not continuous, but interrupted by narrower areas associated with different directions. This pattern is observed for

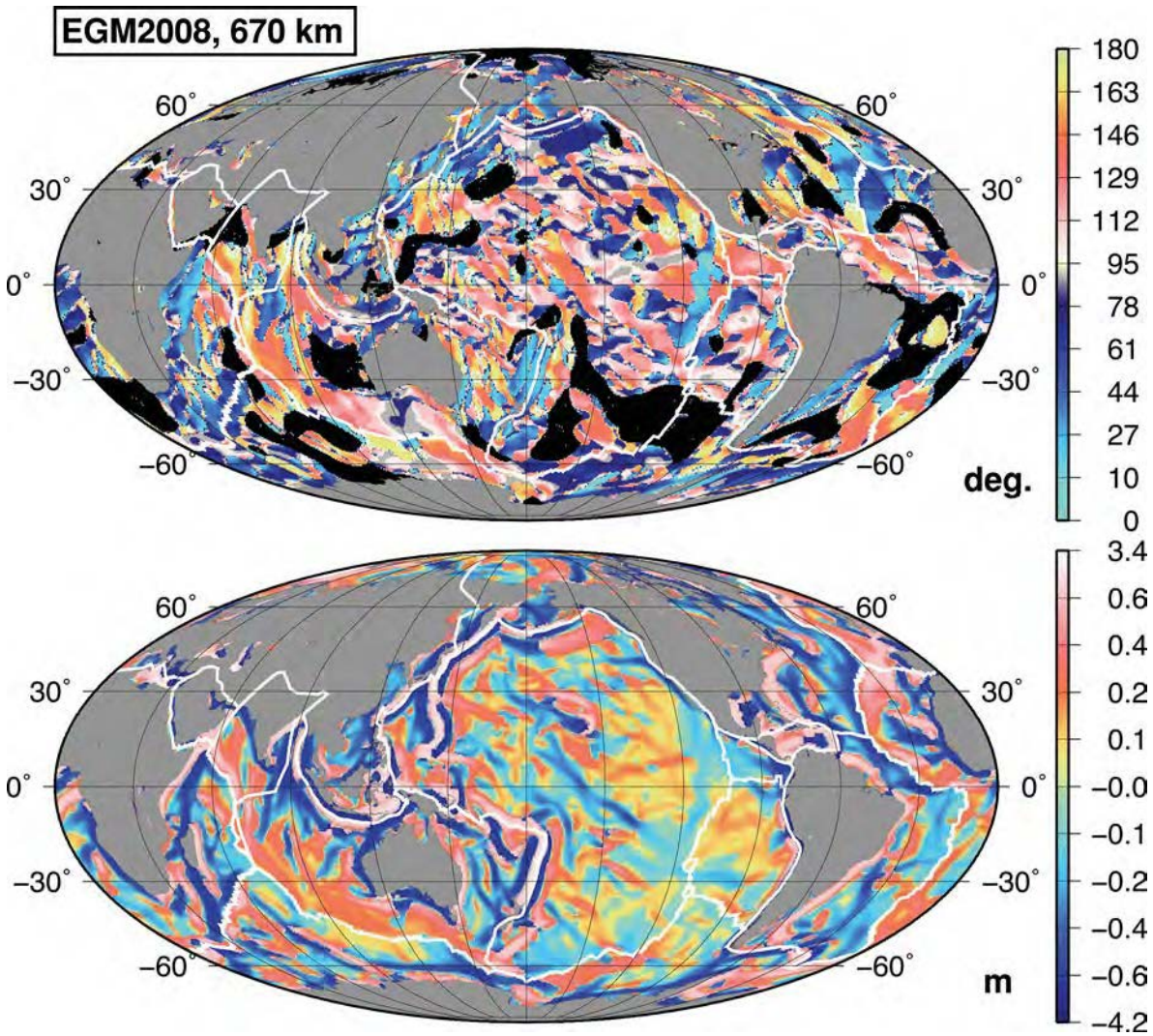

Figure 15. 670 km scale analysis of EGM2008 geoid. Top panel: azimuth of the dominant direction in the wavelet transform; bottom panel: amplitude of the wavelet transform at the dominant direction.

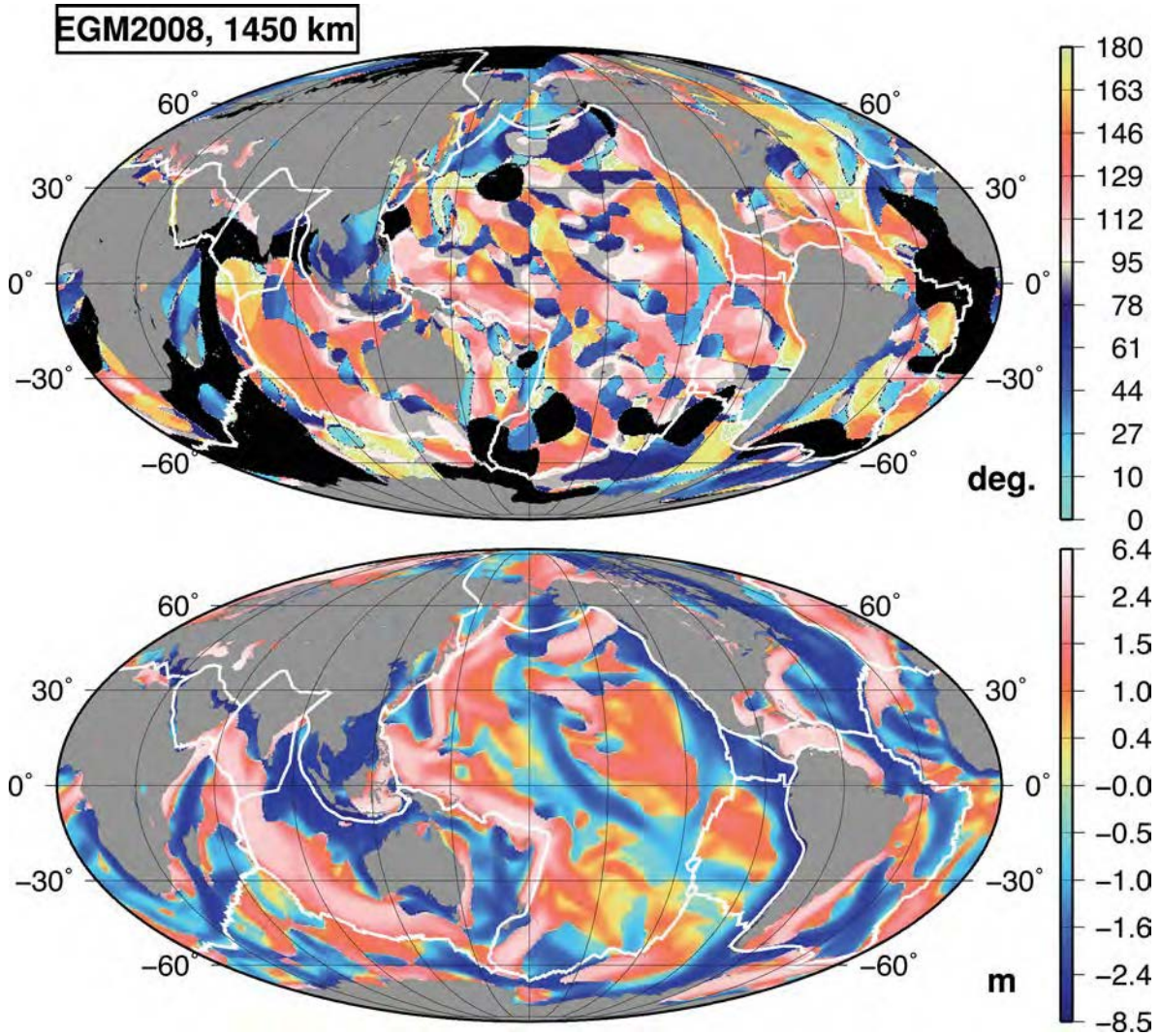

Figure 16. 1450 km scale analysis of EGM2008 geoid. Top panel: azimuth of the dominant direction in the wavelet transform; bottom panel: amplitude of the wavelet transform at the dominant direction.

instance in Fig. 14 (top panel), in the Indian Ocean, where we find a close succession of almost north–south trending lines on the Indo-Australia plate. This case is similar to what is observed in the first synthetic test (Fig. 3). In other cases, large parts of these thinner areas are associated with mostly the same direction. This is observed at small scale in Figs 14 and 18, and at larger scales in Figs 15 to 16 and in Fig. 19, where large NW–SE trending orange lines in the Pacific ocean are often interrupted by blue, NE–SW trending patches. This pattern is similar to what we observe in the synthetic test with the superposition of two loxodroms of different orientations (Fig. 6). In both situations, the discontinuity is due to the fact that the direction is not reliably determined at the location where the CWT amplitude changes its sign, between the succession of a maximum and a minimum associated with a directional undulation. In these 'transition' areas, the observed direction thus no longer corresponds to the orientation of the main local undulation. Either this direction becomes meaningless, or, if a secondary directional system exists at the same location, it will appear and create coherent patterns in these areas.

When noise effects are considered, the entropy mask does not hide it because this noise is superposed to the main undulation, thus lowering the entropy. Moreover, these areas cannot be properly isolated by the amplitude masks based on one unique threshold for all oceans. The reason is as follows. The noise amplitude threshold is quite low as compared to the amplitude of the geoid structures. In areas where the CWT changes its sign, a local threshold based on the amplitude of the local CWT oscillation should be chosen. As geoid features of varying amplitude co-exist in the oceans, the threshold should be adapted area by area, which is difficult to realize in practice. Moreover, a unique threshold based on the dominant geoid signal (subduction zones, typically), can hide all the smaller amplitude patterns. To get the significant but low amplitude features, the threshold needs to be set up low enough, at the cost that non-significant features may appear in areas where the CWT changes its sign.

The above discussion allows us to better understand the significance and patterns present in the maps based on the real data analysis. In addition, to assess the most robust patterns, we increase the amplitude threshold to 10 and 17 per cent of the maximum CWT amplitude at the investigated scale (see Fig. 17) and obtain the results shown in Fig. S2 in the Supporting Information for the larger scales. We note that the NW–SE trending patterns are the major directional system at large scale in the Pacific ocean (orange patches), and that the directions associated with the blue patches,

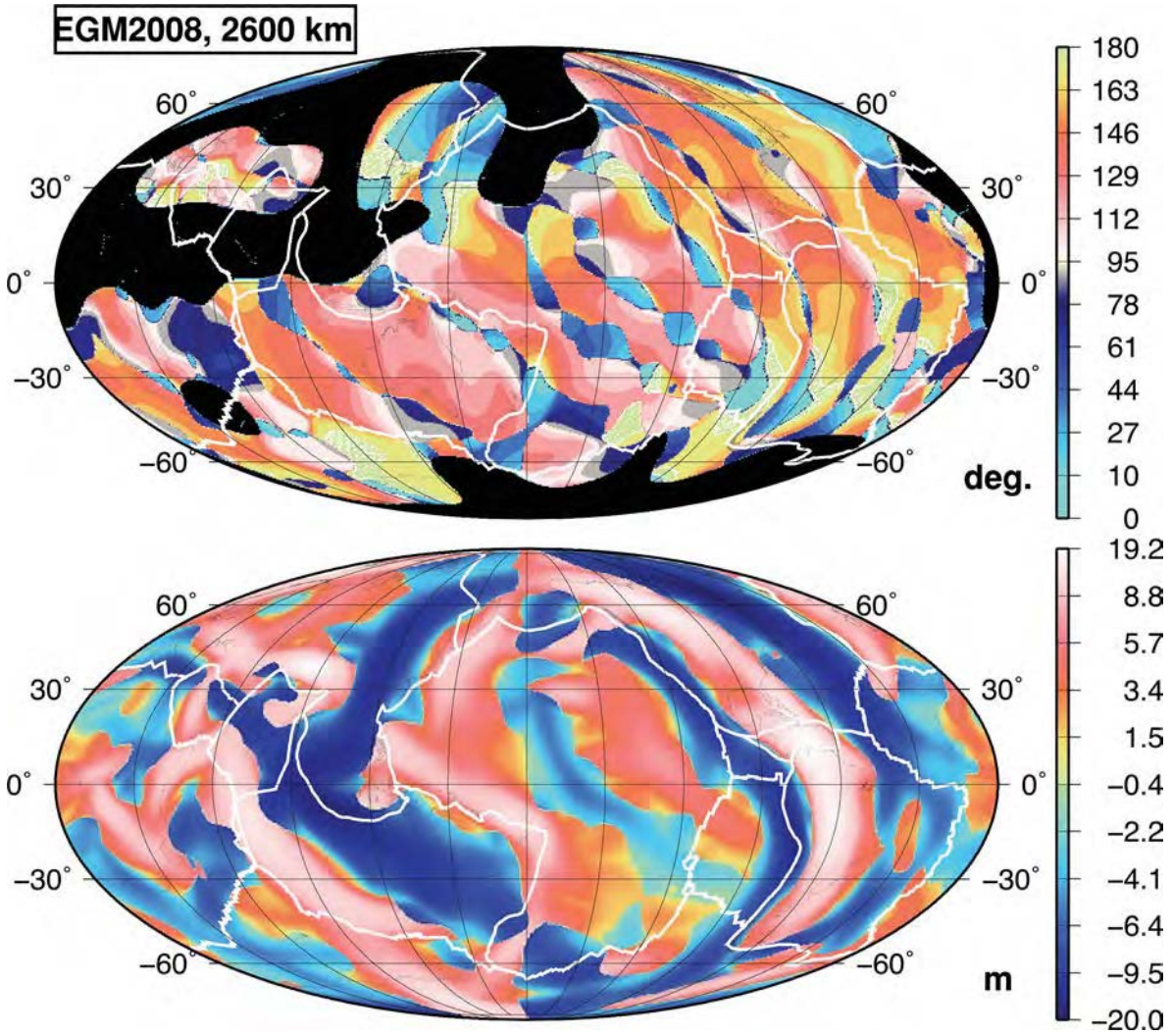

Figure 17. 2600 km scale analysis of EGM2008 geoid. Top panel: azimuth of the dominant direction in the wavelet transform; bottom panel: amplitude of the wavelet transform at the dominant direction.

roughly located in the areas of sign change of the NW–SE patterns, correspond to features of smaller amplitude.

6.2 Directional structures of the geoid

Our results clearly show the presence of elongated patterns in the oceanic geoid. In this section, we describe the observed features, the discussion following in the next section. First, our analysis succeeds in detecting the known tectonic features, such as islands chains and plate boundaries. Their signature in the wavelet transforms is observed in a wide range of scales, with a direction consistent to the alignment or the boundary. For instance, the Mariana, Tonga and Aleutian trenches are clearly visible in Figs 14 (blue lines) and 18. Oceanic ridges are also observed, and the amplitude of the wavelet transforms is consistent with the characteristics of the spreading. Indeed, slow spreading ridges, such as the Atlantic ocean or West Indian Ocean ones, are associated with a rough topography, hence a clear undulation at small scales (Figs 14 and 18), whereas fast spreading ridges, such as the East Pacific Rise, are marked by a smoother topography and the amplitude of their CWT is smaller at small scales. In the Indian ocean, the north–south buckling/folding of the lithosphere and the 90°E ridge are perfectly visible at 200 km scale (Fig. 14). Fracture zones can also be detected in the Pacific ocean, at small scale, although less clearly because they are superimposed onto another set of directional structures that contain much energy at all scales, and are oriented in the 120–140°N direction in the Pacific ocean. All the known tectonic patterns described above create geoid undulations mostly at scales smaller than 500 km, and gradually disappear from the analysis as the scale increases.

On the contrary, the NW–SE trending direction appears more and more strongly in the geoid as the scale increases and crosses the whole Pacific ocean, superimposed to secondary NE–SW trending structures. The amplitude of the secondary undulations is smaller, as shown by the fact that they disappear if the threshold of the amplitude mask is raised (see Fig. S2, Supporting Information). The dominance of this large-scale system of undulations is the major observation we can draw from our analysis. In the bathymetric data, a NW–SE fabric is also visible, but mostly at small scales. As the geoid and bathymetric data sets are fully independent and have different characteristics, the presence of this common orientation in both kinds of data favours a real physical signal and not an artifact.

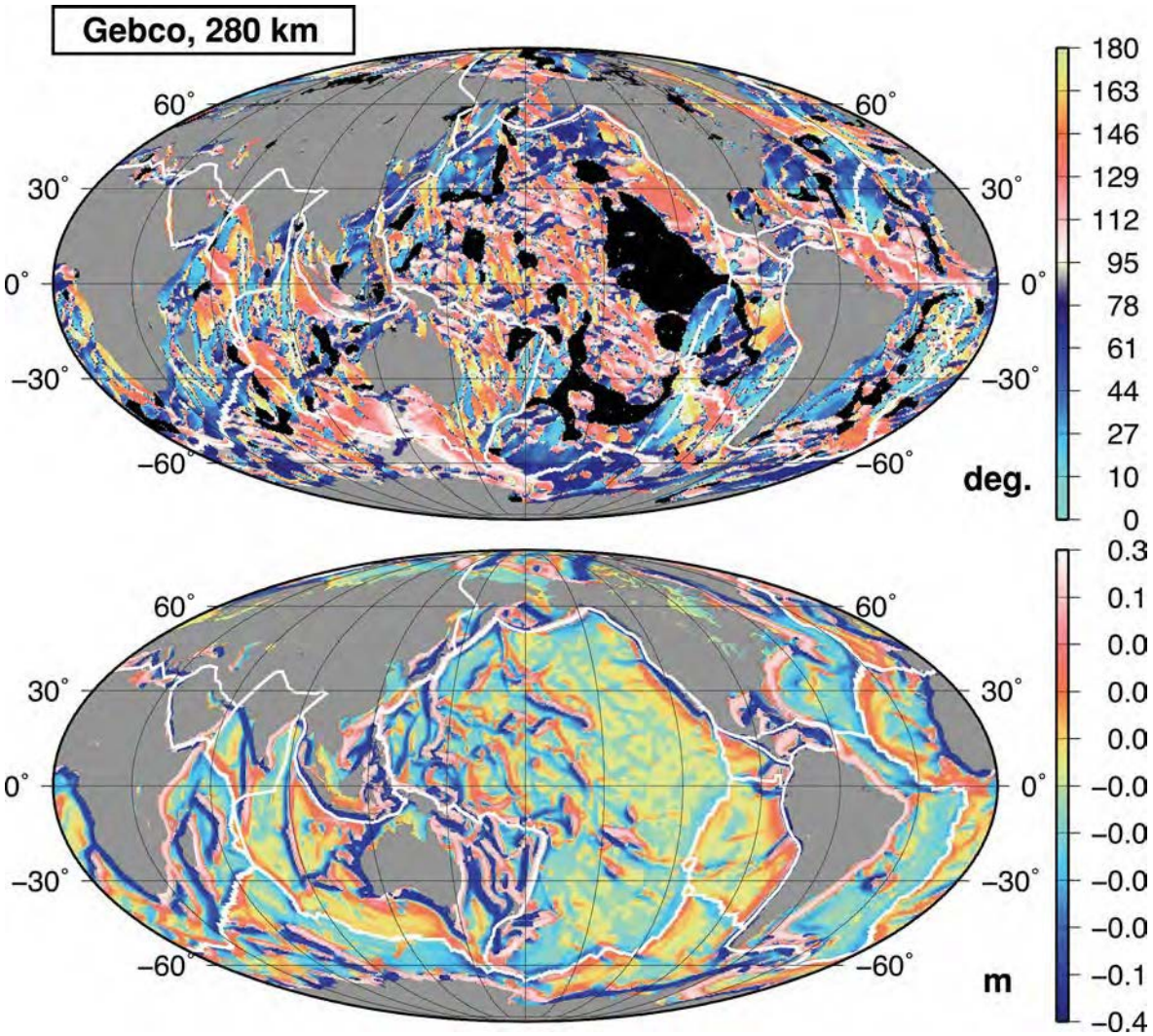

Figure 18. 280 km scale analysis of the geoid effect of Gebco bathymetry. Top panel: azimuth of the dominant direction in the wavelet transform; bottom panel: amplitude of the wavelet transform at the dominant direction.

We speculate that this direction is less clear at large scales in the bathymetric data due to the limited quality of the GEBCO grids in areas where ship cruises are sparse.

We now suggest possible correlations between the NW–SE direction and known geophysical structures.

(1) We first focus on the Pacific ocean and consider the direction of the plate movement. We calculate the correlation of the dominant directions obtained at each location and scale with the azimuth of present day plate motions from the Global Strain Rate Map (GSRM), (Kreemer *et al.* 2003). For that, we evaluate the cosine of the angle between the two directions. The obtained correlation is high for all scales in the Pacific ocean, amounting to about 0.77.

(2) Secondly, the amplitude maps clearly show that this direction persists in the Indian ocean, and seems to cross the ocean/continent limit to continue on the North America plate. Thus, this direction, that coincides with that of the present-day plate motion in most parts of the Pacific ocean, also shows a more global nature. It coincides with the limits of the historic subductions in the mantle that partitions the Earth's mantle into two main boxes (Masters *et al.* 1982; Van Der Hilst *et al.* 1997; Richards & Entgebretson 1982).

(3) We finally note that the direction of the secondary, SW–NE trending undulations could also be related to other limits of the convective box in the mantle below the Pacific ocean.

6.3 Scales of the undulations

To further characterize the undulations detected in the geoid and bathymetry, we investigate their scale. For that, we calculate local wavelet spectra for each location in three major areas shown in Fig. 1: the whole Pacific (lat. −40/40°N, lon. 150/270°E), the South–East Pacific (lat. −40/0°N, lon. 210/270°E) and the North–West Pacific (lat. −10/30°N, lon. 150/210°E). The scaling factors applied to derive the analysis scales are described in Appendix C. We then pick up the scale for which each local spectrum is maximum at each location, and build histograms of distribution of the dominant scales in these investigated areas.

The obtained histograms, represented on Fig. 22, show that the undulated patterns have characteristic scales between 600 and 2000 km for the geoid, and mostly at 600 and 2600 km for the bathymetry. Undulations in the geoid and bathymetry at scales

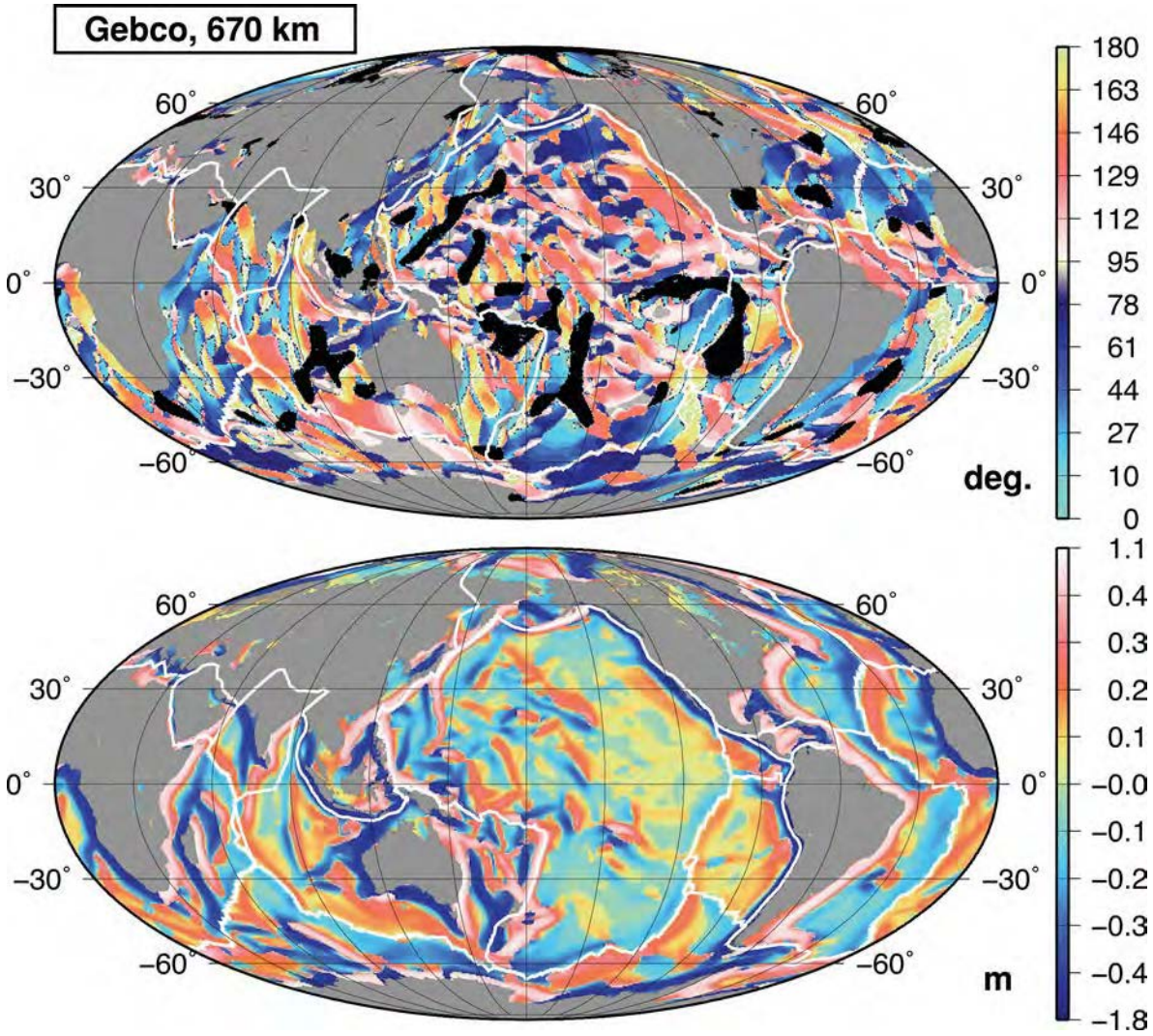

Figure 19. 670 km scale analysis of the geoid effect of Gebco bathymetry. Top panel: azimuth of the dominant direction in the wavelet transform; bottom panel: amplitude of the wavelet transform at the dominant direction.

smaller than 500 km can also be inferred from this analysis, although they appear at the lower limit of our scales range.

(1) In the NE–SW trending directions, we find a 700 km undulation mostly located in the south–east area (P1), likely related to the East Pacific Rise, and a large 1500 km scale geoid structuration in the Pacific ocean (P4), roughly parallel to the East Pacific Rise and to the subduction zone between the Eurasia plate and the Pacific plate, with no clear bathymetric expression.

(2) In the NW–SE trending directions, 600–700 km (P2) and 1200 km (P3) undulations are observed, with a bathymetric expression for P2. A small 2600 km bathymetric structure is also observed in the south–east zone histograms (P6). Finally, the major structure is a 1900 km geoid undulation (P5), with no bathymetric expression, roughly parallel to the limits of the historic subductions in the mantle (North-America/Pacific subduction, Indo-Australie/Antarctic ridge). This structure is particularly clear in the south–east part of the Pacific ocean, where peak P5 is the largest and where the direction maps show most clearly the signal. The north–west, older part of the Pacific plate, shows a more complex histogram, consistent with the fact that it has a more complex directional fabric.

(3) Equatorial directions show a transition between these two systems of undulations.

The amplitude of the undulations is related to the area covered by the associated peak in the histograms. Peak P4 reaches high values, but the associated area may be smaller than for peak P5, which is wider and concentrates more energy, leading to the dominant system of undulations.

Our most striking result is the strong ‘conjugate’ 1500/2000 km peaks in the geoid undulation, particularly clear in the Central and Eastern Pacific (at all latitudes), and in the Eastern Indian ocean, following subduction/accretion directions. In contrast to smaller scale patterns, the NE-SW 2000 km geoid undulations cross the East Pacific Rise (which is associated to a superimposed NS direction). They are also visible in the Indian Ocean. The absence of bathymetric expression for these undulations can either be due to imperfections in the GEBCO bathymetry, which is less precise

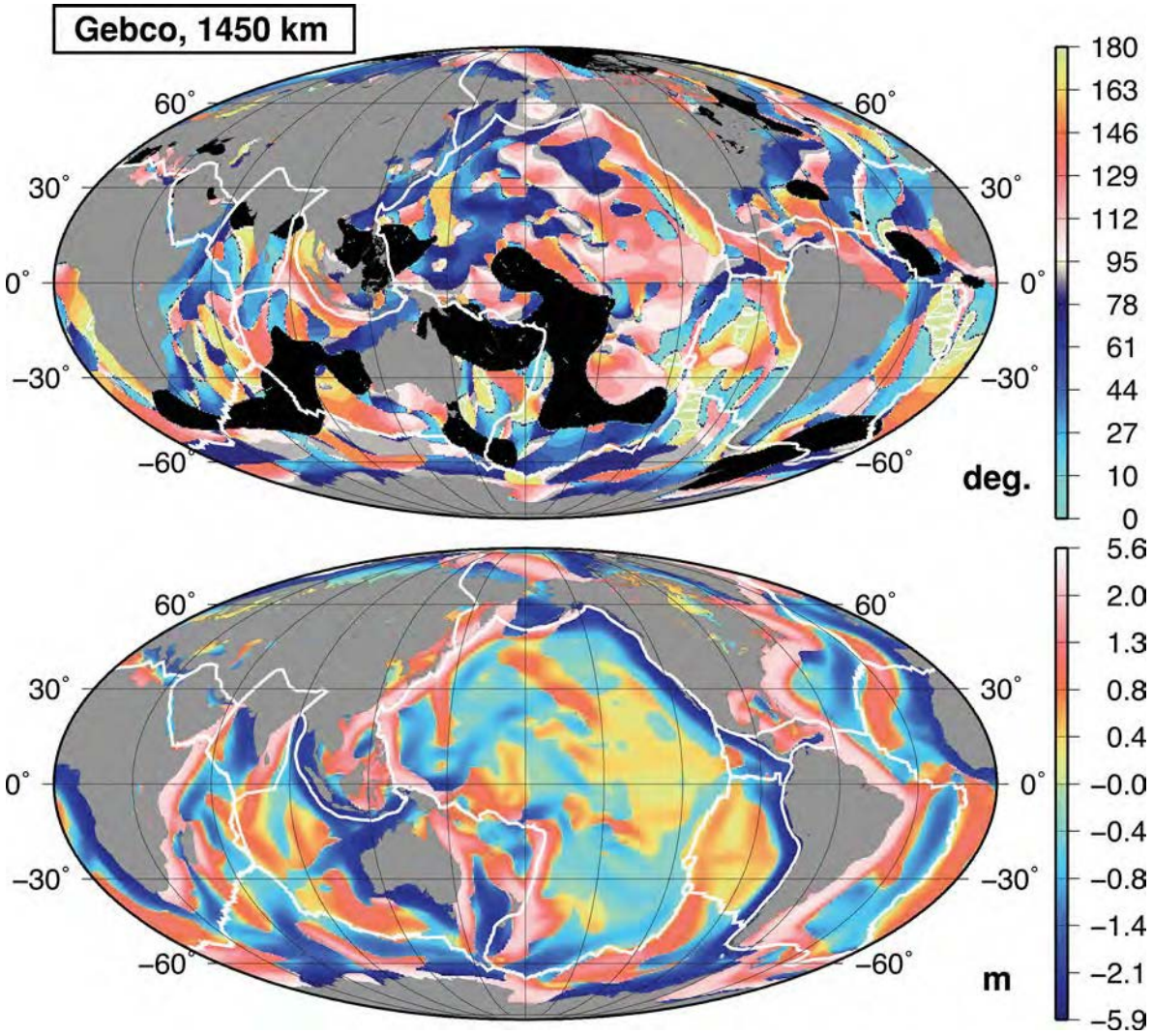

Figure 20. 1450 km scale analysis of the geoid effect of Gebco bathymetry. Top panel: azimuth of the dominant direction in the wavelet transform; bottom panel: amplitude of the wavelet transform at the dominant direction.

at those large scales, or it indicates processes associated with only little amounts of topography, which might suggest different mechanisms to explain the directional structures in the geoid at different scales.

7 DISCUSSION

7.1 Comparison with previous studies

The new analysis of the GRACE-mission-derived geoid models confirms the existence of large-scale directional structures in the oceanic geoid, between 600 and 2000 km scale, some of them having a bathymetric expression. These scales are globally consistent with previous studies and reconcile their conclusions. Indeed, we detect a NW–SE directional structure in most oceanic areas and in a wide range of scales similar to the ones mentioned in papers by Baudry & Kroenke (1991), Maia & Diament (1991) and Cazenave *et al.* (1992). It is the clearest in the fast spreading Pacific ocean. We note that the NW–SE directional pattern is dominant in the Pacific ocean, in agreement with Wessel *et al.* (1994). The SW–NE trending 1500 km scale structures are also consistent with results from Cazenave *et al.* (1992), who observed SW–NE trending directions in the range of 750–1100 km scales in the South–East Pacific, close to the East Pacific Rise. This suggests a network of two superimposed directional fabrics, the main one being oriented in the NW–SE direction.

Our analysis complements the former studies at large scales. In contrast to the mentioned studies, which pre-filtered the data in order to focus on scales smaller than 1400 or 2000 km, no high-pass filter was applied in our study. Thus, undulations at scales larger than 1400 and 2000 km are better described here.

A difference between our results and the above mentioned studies is also observed. Whereas Wessel *et al.* (1994) mention a good coherency between the geoid and the bathymetry at all scales, we find that this coherency degrades for scales larger than about 700 km. This is probably due to the fact that the GRACE data are more sensitive to the deeper contributions to the geoid than the altimetric data used in the previous studies. Consequently, they correlate less with the bathymetry than with the altimetric data. This may also be related to a difference between the ETOPO5 (National Geophysical Data Center 1988), as used by Wessel *et al.* (1994), and GEBCO bathymetric grids.

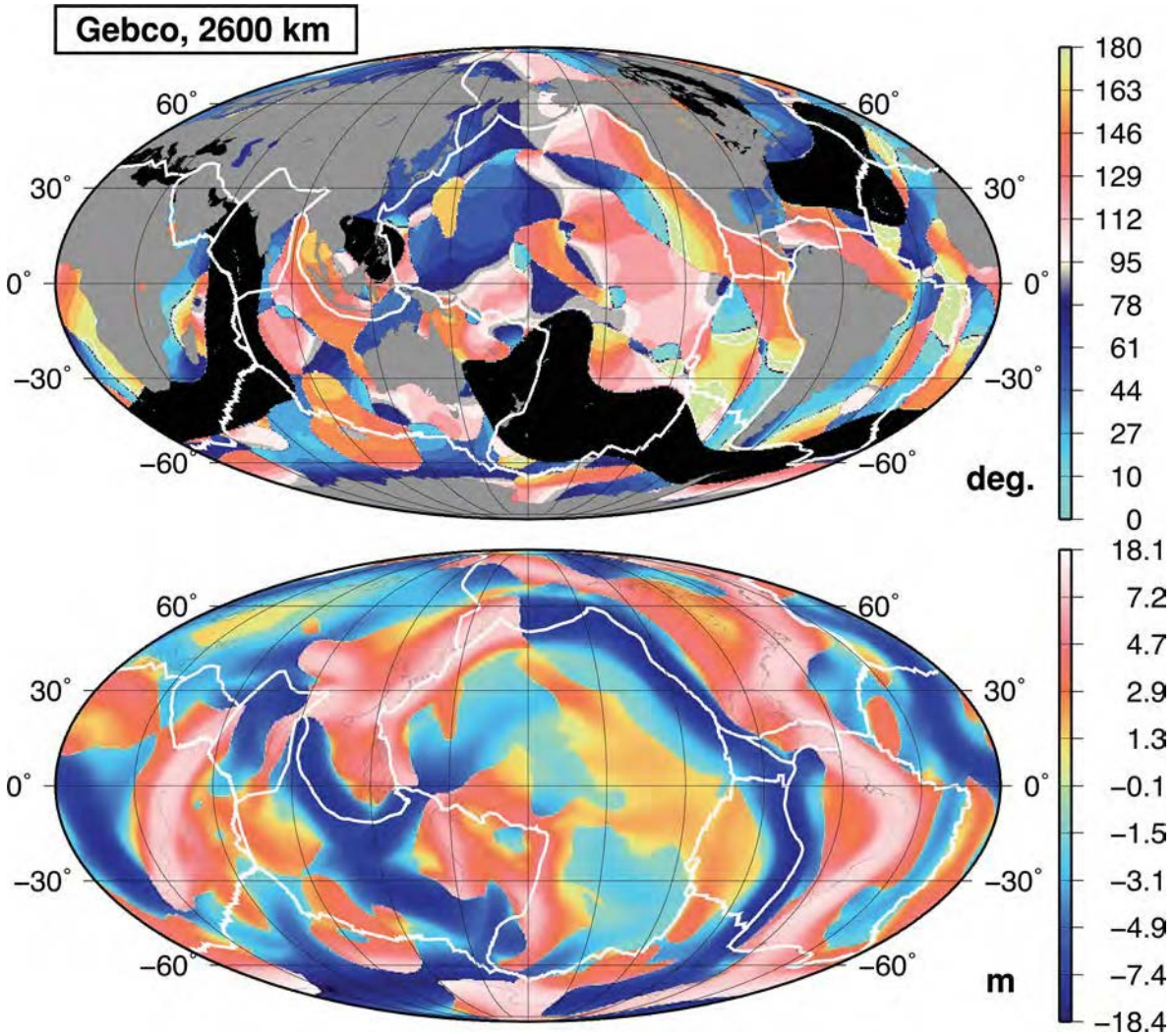

Figure 21. 2600 km scale analysis of the geoid effect of Gebco bathymetry. Top panel: azimuth of the dominant direction in the wavelet transform; bottom panel: amplitude of the wavelet transform at the dominant direction.

7.2 Geodynamic implications

Here we emphasize three possible geodynamic processes which might be responsible for the observed dominant NW–SE 2000 km scale geoid undulations, one of them being more promising. This discussion opens the way to further models and interpretations.

7.2.1 *Lithosphere*

We first consider a purely superficial origin, in which the geoid anomalies are explained by shallow density heterogeneities of large extent localized on, in or just under the lithosphere, such as large islands chains. In this case, the geoid should be strongly correlated with the bathymetry. However, we do not always observe a clear large-scale pattern in the CWT of the gravity potential caused by the bathymetry. Moreover, the geoid undulations cross even the East Pacific Rise. Consequently, if the large-scale geoid undulations are, to some extent, related to superficial structures, the latter are not a sufficient explanation for the whole signal. If they are related to deeper processes, we cannot conclude whether the dynamic topography is small or the Gebco grid not precise enough.

7.2.2 *Secondary convection*

We then consider if secondary convection patterns, related to small-scale geoid undulations (Buck & Parmentier 1986; Robinson & Parsons 1988), can progressively invade the mantle and create large-scale undulations. Secondary convection is indeed known to produce elongated rolls in the direction of plate motion, with wavelengths growing as their mantle penetration depth increases. To obtain rolls over a mantle thickness of about 2000 km, two conditions must be met: (1) the persistence of a given direction of motion of the overriding plate over a very long time, as discussed above, and (2) the existence of quite strong mantle boundaries around 1500/2000 km depth (Richter & Parsons 1975; Parsons & McKenzie 1978; Vidal 2004). However, the direction of motion of the Pacific plate is believed to have changed around 50 Myr ago (e.g. Sharp & Clague 2006), while others suggest no such change in plate motion occurred (e.g. Tarduno *et al.* 2009), and there is no evidence for strong mantle boundaries at 1500 and 2000 km depth. Such elongated rolls should also be detectable by seismic tomography as an alternation of hot and cold regions. However, cross-sections in the recent tomographic models do not confirm this

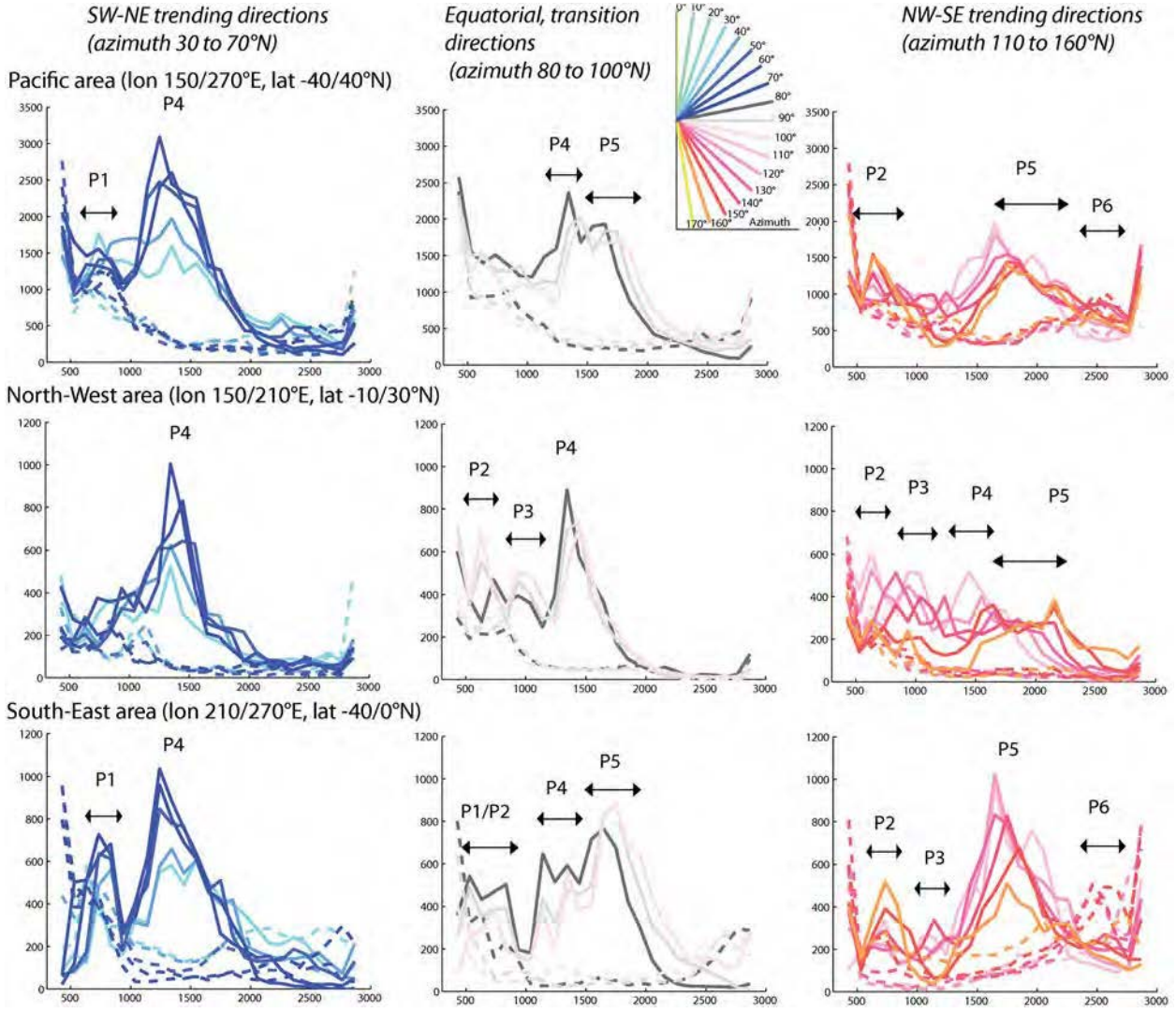

Figure 22. Histograms for three different areas, for the EGM2008 geoid (solid lines) and the geoid effect of the Gebco bathymetry (dashed lines), for selected directions. Each horizontal series of figures corresponds to an area: the Pacific ocean (top panels), the North–West Pacific ocean (middle panels) and the South–East Pacific ocean (bottom panels). The first column corresponds to SE–NW azimuths 30 to 70°N, the second column corresponds to 'transition equatorial' azimuths 80 to 100°N and the last column corresponds to NE–SW azimuths 110 to 160°N. Each line color corresponds to a fixed direction. A few peaks, P_1 to P_6, are indicated.

hypothesis. Consequently, another process affecting the mantle at depth must be invoked.

7.2.3 *Deep mantle upwellings*

The inferred direction not only coincides with the present-day Pacific plate motion, but also with a more global direction observed from the Indian Ocean to the American plate and is consistent with the geometry of present and past subductions. The distribution of the subduction zones and subducting plates cuts the mantle into two boxes, one centred below the Pacific ocean, and the other below the African continent (Masters *et al.* 1982; Richards & Entgebretson 1982; Van Der Hilst *et al.* 1997). The limits of the Pacific mantle box are clearly visible on the geoid map of Fig. 1 and on the CWT amplitude map at 2600 km scale in Fig. 17. They correspond to the NW–SE trending geoid lows around Australia and Northern America. This subduction of the tectonic plates down to the lower mantle strongly structures the deep mantle. Models of thermal convection in a chemically heterogeneous mantle show that thermochemical 3-D instabilities can develop and co-exist and show a wide range of morphologies (Davaille 1999; Le Bars & Davaille 2004), from the classical deep plumes to oscillating domes. Numerical spherical simulations of thermal convection taking into account the present-day distribution of subduction zones, the effect of plate motion and subduction inside the mantle, further show that the hot material can then be confined into preferentially elongated structures (McNamara & Zhong 2005; Quéré & Forte 2006). Given the size of these hot structures, laboratory experiments predict that they should generate several 3-D hot instabilities (Davaille *et al.* 2005). This view is confirmed by the tomographic models, which all show several seismic slow extrema in the Pacific and African boxes, linked to 3-D slow structures higher up in the mantle (Ritsema & Van Heijst 2000; Gu *et al.* 2001; Romanowicz & Gung 2002; Davaille *et al.* 2005; Forte *et al.* 2010). This is also what we begin to see in the electrical conductivity model for the lower mantle of Tarits & Mandea (2010), although the resolution needs to be improved. Some large-scale common (low conductivity—high velocity) features can be observed, one being just in the middle of the Pacific ocean

with a NW–SE orientation. To explain our observations of geoid undulations at 2000 km scale, we thus propose a hybrid model involving two steps.

(1) In the first step, several 3-D hot instabilities are formed in the deep mantle, with a large scale spacing influenced by the distribution of the subduction zones and subducting plates within the mantle and leading to a directional distribution of the instabilities.

(2) In a second step, the impact of these instabilities under the lithosphere produces hot spot volcanism and hot elongated puddles of hot material into the asthenosphere, which is carried away by plate motion.

The geoid, being the sum of the two contributions, is then showing a pattern of bands elongated in the direction of plate motions: this is what we observe. The Pacific plate is purely oceanic and has a fast movement with respect to the mantle, contrary to the African plate. This is the reason why the geoid signature of this process is more clearly seen over the Pacific convective box, but we conceive that this is a global phenomenon associated to the global dynamics of our planet.

8 CONCLUSION

In this paper, we present a new directional wavelet analysis of the geopotential using directional Poisson wavelets. This method allows us to highlight elongated structures in the Earth's gravity potential in a clearer way than using isotropic wavelets and to relate them to variations in the density of the Earth's interior. We compute significance tests by comparing the amplitude and the entropy of the directional distribution of the wavelet coefficients to those of a reference noise model. These tests allow us to interpret only the directional structures that can be distinguished from the noise with a high confidence level. Local spectra allow us to assess the characteristic scale of these structures.

We apply the directional wavelet analysis to recent gravity models based on the GRACE data and independent bathymetry data. The high precision and accuracy of the GRACE data at wavelengths larger than 200 km allow us to revisit the question of the existence and characteristics of large-scale undulations in the oceanic geoid, previously evidenced in satellite altimetry data.

Our analysis confirms the existence of large-scale undulations in the geoid over the oceans, with scales ranging from 600 to 2000 km. The major undulations have a 2000 km scaling and their NW–SE orientation correlates well with the present day plate movement in the Pacific ocean. They are associated with a conjugate SW–NE secondary pattern at 1500 km scale. The presence of a bathymetric signature for the 600 km scale undulations rules out the possibility of data analysis artefact.

The major 2000 km scale NW–SE directional fabric appears to be global, and consistent with the geometry of present and past subduction. To explain it, we propose a hybrid model in two steps. In a first step, 3-D hot instabilities are generated in the deep mantle with a spacing and directional distribution constrained by the geometry of the subducted plates inside the mantle. In a second step, these instabilities impact the lithosphere and are carried away by plate motion. We propose that this process is global, indicating a global mantle structure, particularly visible in the Pacific. Further studies will be necessary to confirm and refine this proposed model, and account for our observations in a more precise and detailed way.

ACKNOWLEDGMENTS

We thank Jean Besse for fruitful discussions on these results, and Cecilia Cadio for commenting our manuscript. We thank the Editor, Jun Korenaga, and two anonymous reviewers, for their insightful comments that contributed to improve our manuscript. This work was supported by CNES through the TOSCA committee. All maps were plotted using the GMT software (Wessel & Smith 1995). This is IPGP contribution 3283.

REFERENCES

Audet P., 2011. Directional wavelet analysis on the sphere: application to gravity and topography of the terrestrial planets, *J. geophys. Res.*, **116,** E01003, doi:10.1029/2010JE003710.

Baudry, N. & Diament, M., 1987. Shipboard confirmation of Seasat bathymetric predictions in the South Central Pacific, in *Seamounts, Islands, and Atolls*, Geophys. Monogr. Ser. Vol 43, pp. 115–122, eds Keating, B.H., *et al.*, American Geophysical Union, Washington D.C.

Baudry, N., Diament, M. & Albouy, Y., 1987. Precise location of unsurveyed seamounts in the Austral archipelago area using SEASAT data, *Geophys. J. R. Astr. Soc.*, **89**(3), 869–888.

Baudry, N. & Kroenke, L., 1991. Intermediate-wavelength (400–600 km), South Pacific geoidal undulations: their relationship to linear volcanic chains, *Earth planet. Sci. Lett.*, **102,** 430–443.

Biancale, R. *et al.*, 2010. Seven years of gravity variations from GRACE and LAGEOS data from CNES/GRGS, http://grgs.obs-mip.fr/index.php/fre/Donnees-scientifiques/Champ-de gravite/grace.

Buck, W.R. & Parmentier, E.M., 1986. Convection beneath young oceanic lithosphere: implications for thermal structure and gravity, *J. geophys. Res.*, **91,** 1961–1974.

Cadio, C., Panet, I., Davaille, A., Diament, M., Metivier, L. & de Viron, O., 2011. Pacific geoid anomalies revisited in light of thermochemical oscillating domes in the lower mantle, *Earth planet. Sci. Lett.*, **306,** 123–135.

Cazenave, A., Monnereau, M. & Gibert, D., 1987. Seasat gravity undulations in the central Indian Ocean, *Phys. Earth planet. Inter.*, **48,** 130–141.

Cazenave, A., Houry, S., Lago, B. & Dominh, K., 1992. Geosat-derived geoid anomalies at medium wavelength, *J. geophys. Res.*, **97,** 7081–7096.

Chambodut, A., Panet, I., Mandea, M., Diament, M., Holschneider, M. & Jamet O., 2005. Wavelet frames: an alternative to spherical harmonic representation of potential fields, *Geophys. J. Int.*, **3,** 875–899, doi:10.1111/j.1365-246X.2005.02754.x.

Chen, J.L., Wilson, C.R., Famiglietti, J.S. & Rodell, M., 2005. Spatial sensitivity of the gravity recovery and climate experiment (GRACE) time-variable gravity observations, *J. Geophys. Res.*, **110,** B08408.

Davaille, A., 1999. Simultaneous generation of hotspots and superswells by convection in a heterogeneous planetary mantle, *Nature*, **402,** 756–760.

Davaille, A., Stutzmann, E., Silveira, G., Besse, J. & Courtillot, V., 2005. Convective patterns under the Indo Atlantic "box", *Earth planet. Sci. Lett.*, **239,** 233–252.

Dunbar, J. & Sandwell, D.T., 1988. A boudinage model for crossgrain lineations, *EOS, Trans. Am. geophys. Un.*, **69,** 1429.

Fleitout, L., Dalloubeix, C. & Moriceau, C., 1989. Small-wavelength geoid and topography anomalies in the South Atlantic Ocean – a clue to new hot-spot tracks and lithospheric deformation, *Geophys. Res. Lett.*, **16,** 637–640.

Fleitout, L. & Moriceau, C., 1992. Short-wavelength geoid, bathymetry and convective pattern beneath the Pacific ocean, *Geophys. J. Int.*, **110,** 6–28.

Foerste, C. *et al.*, 2008. The GeoForschungsZentrum Potsdam/Groupe de Recherche de Geodesie Spatiale satellite-only and combined gravity field models: EIGEN-GL04S1 and EIGEN-GL04C. *J. Geod.*, **82**(6), 331–346.

Forte, A.M. & Mitrovica, J., 2001. Deep-mantle high-viscosity flow and thermochemical structure inferred from seismic and geodynamic data, *Nature*, **410,** 1049–1056.

Forte, A.M., Quéré, S., Moucha, R., Simmons, N.A., Grand, S.P., Mitrovica, J.X. & Rowley, D.B., 2010. Joint seismic-geodynamic-mineral physical

modelling of African geodynamics: A reconciliation of deep-mantle convection with surface geophysical constraints, *Earty planet. Sci. Lett.*, **259**(3–4), 329–341.
IOC, IHO and BODC. 2003. Centenary edition of the GEBCO digital atlas, published on CD-ROM on behalf of the Intergovernmental Oceanographic Commission and the International Hydrographic Organization as part of the General Bathymetric Chart of the Oceans; British Oceanographic Data Centre, Liverpool.
Gu, Y., Dziewonski, A., Su, W. & Ekstrom, G., 2001. Models of the mantle shear velocity and discontinuities in the pattern of lateral heterogeneities, *J. geophys. Res.*, **106**(B6), 11 169–11 199.
Hager, B.H., Clayton, R.W., Richards, M.A., Comer, R.P. & Dziewonski, A.M., 1985. Lower mantle heterogeneity, dynamic to- pography and the geoid, *Nature*, **313,** 541–545.
Hager, B.H. & Richards, M.A., 1989. Long-wavelength variations in earth's geoid – physical models and dynamical implications, *Philos. Trans. R. Soc. Lond. A*, **328,** 309–327.
Haxby, W.F. & Weissel, J.K., 1986. Evidence for small-scale convection from Seasat altimeter data, *J. geophys. Res.*, **91,** 3507–3520.
Haxby, W.F., Labrecque, J.L., Weissel, J.K. & Karner, G., 1983. Digital images of combined oceanic and continental data sets and their use in tectonic studies, *EOS, Trans. Am. geophys. Un.*, **64,** 995–1004
Hayn, M. & Holschneider, M., 2009. Directional spherical multipole wavelets, *J. Math. Phys.*, **50**(7), 073512–073512, doi:10.1063/1.3177198.
Holschneider, M., 1996. Continuous wavelet transforms on the sphere, *J. Math. Phys.*, **37,** 4156.
Iglewska-Nowak, I. & Holschneider, M., 2007. Poisson wavelets on the sphere, *J. Four. Anal. Appl.*, **13**(4), 405–419.
Kreemer, C., Holt, W.E. & Haines, A., 2003. An integrated global model of present-day plate motions and plate boundary deformation, *Geophys. J. Int.*, **154,** 8–34.
Landsberg, P.T., 1984. Can entropy and "order" increase together? *Phys. Lett. A*, **102A**(4), 171–173.
Le Bars, M. & Davaille, A., 2004. Whole layer convection in a heterogeneous planetary mantle, *J. geophys. Res.*, **109,** B03403. doi:10.1029/2003JB002617.
Maia, M. & Diament, M., 1991. An analysis of the altimetric geoid in various wavebands in the central Pacific ocean: constraints on the origin of intraplate features, *Tectonophysics*, **190,** 133–153.
Masters, G., Jordan, T.H., Silver, P.G. & Gilbert, F., 1982. A spherical Earth structure from fundamental spheroidal-mode data, *Nature*, **298,** 609–613.
McNamara, A.K. & Zhong, S., 2005. Thermochemical structures beneath Africa and the Pacific ocean, *Nature*, **437,** 1136–1139, doi:10.1038/nature04066
Müller, R.D., Roest, W.R., Royer, J.-Y., Gahagan, L.M. & Sclater, J.G., 1997. Digital isochrons of the world's ocean floor, *J. geophys. Res.*, **102**(B2), 3211–3214.
National Geophysical Data Center, 1988. ETOPO-5 Bathymetry/ Topography data, Data announcement 88-MG-02, National Oceanic and Atmospheric Administration, U.S. Dept. of Commerce.
Panet, I., Chambodut, A., Diament, M., Holschneider, M. & Jamet, O., 2006. New insights on intra-plate volcanism in French Polynesia from wavelet analysis of GRACE, CHAMP and sea-surface data, *J. geophys. Res.*, **111,** B09403, doi:10.1029/2005JB004141.
Parsons, B. & McKenzie, D.P., 1978. Mantle convection and the thermal structure of the plates, *J. geophys. Res.*, **82,** 4485–4495.
Pavlis, N.K., Holmes, S.A., Kenyon, S.C. & Factor, J.K., 2008. An earth gravitational model to degree 2160: EGM2008, *Geophys. Res. Abstr.*, **10,** EGU2008-A-01891.
Pavlis, N.K. & Holmes, S.A., 2004. A preliminary gravitational model to degree 2160, in *Gravity, Geoid and Space Missions*, GGSM 2004 IAG International Symposium, Porto, 2004 August 30–September 3, eds Jekeli, C., Bastos, L. & Fernandes, J., Springer, Berlin.
Quéré, S. & Forte, A., 2006. Influence of past and present-day plate motions on spherical models of mantle convection: implications for mantle plumes and hotspots, *Geophys. J. Int.*, **165,** 1041–1057, doi:10.1111/j.1365-246X.2006.02990.x.
Ricard, Y. & Wuming, B., 1991. Inferring the viscosity and the 3-D density structure of the mantle from geoid, topography and plate velocities, *Geophys. J. Int.*, **105,** 561–571.
Richards, M.A., Entgebretson, D.C., 1992. Large-scale mantle convection and the history of subductions, *Nature*, **355,** 437–440.
Richter, F. & Parsons, B., 1975. On the interaction of two scales of convection in the mantle, *J. geophys. Res.*, **80,** 2529–2541.
Ritsema, J. & van Heijst, H.J., 2000. Seismic imaging of structural heterogeneity in Earth's mantle: evidence for large-scale mantle flow, *Sci. Progr.*, **83,** 243–259.
Robinson, E. & Parson, B., 1988. Effect of a shallow low-viscosity zone on small-scale instabilities under the cooling oceanic plates, *J. geophys. Res.*, **93,** 3469–3479.
Romanowicz, B. & Gung, Y., 2002. Superplumes from the core-mantle boundary to the lithosphere: implications for heat flux, *Science*, **296,** 513–516.
Sandwell, D. & Fialko, Y., 2004. Warping and cracking of the Pacific plate by thermal contraction, *J. geophys. Res.*, **109,** B10411, doi:10.1029/2004JB003091.
Sharp, W.D. & Clague, D.A., 2006. 50-Ma initiation of Hawaiian-emperor bend records major change in Pacific plate motion, *Science*, **313**(5791), 1281–1284.
Swenson, S. & Wahr, J., 2006. Post-processing removal of correlated erros in GRACE data, *Geophys. Res. Lett.*, **33,** L08402.
Tapley, B.D., Bettadbur, S., Watkins, M. & Reigberg, C., 2004. The gravity recovery and climate experiment: mission overview and early results, *Geophys. Res. Lett.*, **31**(9), L09607, doi:10.1029/2004GL019920.
Tapley, B., Ries, J., Bettadpur, S., Chambers, D., Cheng, M., Condi, F. & Poole, S., 2007. The GGM03 mean Earth gravity model from GRACE, *EOS, Trans. Am. Geophys. Un.*, **88**(52), Fall Meet. Suppl., Abstract G42A-03.
Tarduno, J., Bunge, H.-P., Sleep, N. & Hansen, U., 2009. The bent Hawaiian-emperor hotspot track: inheriting the mantle wind, *Science*, **324**(5923), 50–53.
Tarits, P. & Mandea, M., 2010. The heterogeneous electrical conductivity structure of the lower mantle, *Phys. Earth planet. Inter.*, **183**(1–2), 115–125.
Van Der Hilst, R., Widiyantoro, S. & Engdahl, E.R., 1997. Evidence for deep mantle circulation from global tomography, *Nature*, **386,** 578–584.
Vidal, V., 2004. Interaction des diffrentes chelles de convection dans le manteau terrestre, *PhD thesis*, Institut de Physique du Globe de Paris.
Wessel, P., Bercovici, D. & Kroenke, L., 1994. The possible reflection of mantle discontinuities in Pacific geoid and bathymetry, *Geophys. Res. Lett.*, **21**(18), 1943–1946.
Wessel, P. & Smith, W.H.F., 1995. New version of the generic mapping tool, *EOS, Trans. Am. geophys. Un.*, **76**(33), 329, doi:10.1029/95EO00198.

APPENDIX A: CWT OF THE GRAVITY POTENTIAL: LINK TO DENSITIES

Here we provide the analytical expression of the CWT of the gravity potential with directional Poisson wavelets and its relation to the density distribution inside the Earth. Let us denote the gravity potential $\Phi(\boldsymbol{y})$ at the point $\boldsymbol{y}$ as:

$$\Phi(\boldsymbol{y}) = G\int_{V_E} d^3\boldsymbol{x}\ \frac{\rho(\boldsymbol{x})}{|\boldsymbol{x}-\boldsymbol{y}|},$$

with ρ being the Earth's density and V_E the Earth's volume. G is the gravitational constant, approximately equal to $6.67 \times 10^{-11}\,\mathrm{m^3\,kg^{-1}\,s^{-2}}$. Its wavelet transform by the wavelet ψ_a^n at scale a, direction azimuth α and position (ϑ, φ) reads:

$$\mathcal{W}_{\{\psi_a^n\}}\Phi(a,\alpha,\vartheta,\varphi) = \frac{1}{R_E^2}\int_{\Sigma_E} d\mu(\boldsymbol{y})\Phi(\boldsymbol{y})\mathcal{R}(\alpha)\mathcal{T}(\vartheta,\varphi)\psi_a^n(\boldsymbol{y}) \quad \text{(A1)}$$

where Σ_E is the mean Earth sphere of radius R_E and $d\mu(\boldsymbol{y})$ is the surface element of this sphere at position $\boldsymbol{y}$.

We now show that the wavelet transform of the gravity potential in eq. (A1) is equal to the integral of the densities inside the Earth, weighted with a multipole weighting function. The wavelet is defined on the Earth's surface as:

$$\psi_a^n(\boldsymbol{y}) = \partial_\xi^n \mathcal{T}_{\hat{\boldsymbol{e}}_z}(\xi, 0) a^n \sum_l e^{-al} Q_l(\hat{\boldsymbol{y}} \cdot \hat{\boldsymbol{e}}_z)$$

where $Q_l = (2l+1)P_l$ and P_l is the Legendre polynomial of degree l. For the evaluation of the wavelet, only the direction of $\boldsymbol{y}$ is considered, using the unit vector $\hat{\boldsymbol{y}} = \boldsymbol{y}/\|\boldsymbol{y}\|$. The function $\frac{1}{|\boldsymbol{x}-\boldsymbol{y}|}$ has the Legendre expansion for $|\boldsymbol{x}| < |\boldsymbol{y}|$:

$$\frac{1}{|\boldsymbol{x}-\boldsymbol{y}|} = \frac{1}{|\boldsymbol{y}|} \sum_{l\geq 0} \left(\frac{|\boldsymbol{x}|}{|\boldsymbol{y}|}\right)^l P_l(\hat{\boldsymbol{x}} \cdot \hat{\boldsymbol{y}}). \tag{A2}$$

Let us insert these two expression in the eq. (A1) defining the wavelet transform of the gravity potential. Taking into account the orthogonality property of the Legendre polynomials of different degrees:

$$\int_\Omega Q_l(\hat{\boldsymbol{x}} \cdot \hat{\boldsymbol{y}}) P_{l'}(\hat{\boldsymbol{x}} \cdot \hat{\boldsymbol{y}}') d\mu(\hat{\boldsymbol{x}}) = \delta_{ll'} P_l(\hat{\boldsymbol{y}} \cdot \hat{\boldsymbol{y}}'),$$

we end up with:

$$\begin{aligned}
&\mathcal{W}_{\{\psi_a^n\}}\Phi(a, \alpha, \vartheta, \varphi) \\
&\quad = G \int_{V_E} d^3\boldsymbol{x}\, \delta\rho(\boldsymbol{x}) \dots \\
&\quad \dots \mathcal{R}(\alpha)\mathcal{T}(\vartheta, \varphi)\partial_\xi^n \mathcal{T}_{\hat{\boldsymbol{e}}_z}(\xi, 0) \frac{a^n}{R_E} \sum_l e^{-al} \left(\frac{|\boldsymbol{x}|}{R_E}\right)^l P_l(\hat{\boldsymbol{x}} \cdot \hat{\boldsymbol{e}}_z).
\end{aligned}$$

Applying again the Legendre expansion (A2), this can be rewritten as:

$$\mathcal{W}_{\{\psi_a^n\}}\Phi(a, \alpha, \vartheta, \varphi) = G \int_{V_E} d^3\boldsymbol{x}\, \delta\rho(\boldsymbol{x}) \mathcal{R}(\alpha)\mathcal{T}(\vartheta, \varphi) F_a^n(\boldsymbol{x})$$

where the densities are weighted with the multipole weighting function:

$$F_a^n(\boldsymbol{x}) = \partial_\xi^n \mathcal{T}_{\hat{\boldsymbol{e}}_z}(\xi, 0) a^n e^a \frac{1}{\left|\boldsymbol{x} - R_E e^a \hat{\boldsymbol{e}}_z\right|}.$$

APPENDIX B: CWT OF THE GEOID EFFECT OF THE BATHYMETRY

Here we derive the analytical expressions for the CWT of the gravity potential associated with the bathymetry, using directional Poisson wavelets. We calculate the contribution to the geoid of the bathymetry in spherical geometry following Panet *et al.* (2006). The principle consists in calculating the difference of gravity potential between an ideal ellipsoidal solid Earth with radial layers of constant densities, and a real Earth where the presence of the oceans above the bathymetry creates a mass anomaly. The associated density anomalie $\delta\rho$ is assumed to be approximately constant at $-1700\ \mathrm{kg\,m^{-3}}$, that is the difference between the density $2700\ \mathrm{kg\,m^{-3}}$ in the model Earth crust and the density of water. To calculate the gravity effect of this source, we make the assumption that all the ocean and bathymetry masses are enclosed in a thin layer at the surface of the Earth. This hypothesis is valid in the range of investigated geoid undulations scales (larger than 200 km). We thus define a surface load associated to the bathymetry as:

$$\int_{r=R_E-H(\hat{\boldsymbol{x}})}^{R_E} dr\ \delta\rho(r\hat{\boldsymbol{x}}) =: \Delta\sigma(\hat{\boldsymbol{x}}). \tag{B1}$$

where $H(\hat{\boldsymbol{x}})$ is the bathymetric depth. Note that, on land, a topographic load can be defined in the same way as:

$$\int_{r=R_E}^{R_E+H(\hat{\boldsymbol{x}})} dr\ \delta\rho(r\hat{\boldsymbol{x}}) =: \Delta\sigma(\hat{\boldsymbol{x}}). \tag{B2}$$

and in this case, $\delta\rho$ is the crustal density ($2700\ \mathrm{kg\,m^{-3}}$).

The gravity potential which arises from the bathymetry is denoted by $\Delta\Phi$ and is equal to

$$\Delta\Phi(\boldsymbol{y}) = G \int_{\Sigma_E} d\mu(\hat{\boldsymbol{x}}) \int_{r=R_E-H(\hat{\boldsymbol{x}})}^{R_E} dr\, \frac{\delta\rho(r\hat{\boldsymbol{x}})}{|r\hat{\boldsymbol{x}} - \boldsymbol{y}|}.$$

For the wavelet transform of $\Delta\Phi$ we get:

$$\begin{aligned}
&\mathcal{W}_{\{\psi_a^n\}}\Delta\Phi(a, \alpha, \vartheta, \varphi) \\
&\quad = G \int_\Omega d\mu(\hat{\boldsymbol{x}}) \int_{r=R_E-H(\hat{\boldsymbol{x}})}^{R_E} dr\, r^2 \delta\rho(r\hat{\boldsymbol{x}}) \dots \\
&\quad \dots \mathcal{R}(\alpha)\mathcal{T}(\vartheta, \varphi)\partial_\xi^n \mathcal{T}_{\hat{\boldsymbol{e}}_z}(\xi, 0) \frac{a^n}{R_E} \sum_l e^{-al} \left(\frac{r}{R_E}\right)^l P_l(\hat{\boldsymbol{x}} \cdot \hat{\boldsymbol{e}}_z).
\end{aligned}$$

Inserting the bathymetry density load (B1) and approximating $r/R_E \approx 1$ results in:

$$\begin{aligned}
&\mathcal{W}_{\{\psi_a^n\}}\Delta\Phi(a, \alpha, \vartheta, \varphi) \\
&\quad = G \int_\Omega d\mu(\hat{\boldsymbol{x}})\ \Delta\sigma(\hat{\boldsymbol{x}}) \dots \\
&\quad \dots \mathcal{R}(\alpha)\mathcal{T}(\vartheta, \varphi)\partial_\xi^n \mathcal{T}_{\hat{\boldsymbol{e}}_z}(\xi, 0) R_E a^n \sum_l e^{-al} P_l(\hat{\boldsymbol{x}} \cdot \hat{\boldsymbol{e}}_z).
\end{aligned}$$

Using again the Legendre expansion (A2) of $\frac{1}{|\boldsymbol{x}-\boldsymbol{y}|}$, we end up with:

$$\mathcal{W}_{\{\psi_a^n\}}\Delta\Phi(a, \alpha, \vartheta, \varphi) = G R_E \left\langle \Delta\sigma \,|\, \mathcal{R}(\alpha)\mathcal{T}(\vartheta, \varphi) F_a^n \right\rangle$$

with the multipole weighting function:

$$F_a^n(\hat{\boldsymbol{x}}) = \partial_\xi^n \mathcal{T}_{\hat{\boldsymbol{e}}_z}(\xi, 0) a^n e^a \frac{1}{|\hat{\boldsymbol{x}} - e^a \hat{\boldsymbol{e}}_z|}.$$

This relation was already shown in Panet *et al.* (2006) for isotropic Poisson wavelets. In this case, the multipole weighting functions are axial multipoles arising from radial derivations $\partial_{|\boldsymbol{x}|}$ of the potential $\frac{1}{|\boldsymbol{x}-\boldsymbol{y}|}$. By analogy, the multipole weighting functions corresponding to directional Poisson wavelets can be derived as multipoles arising from rotational derivations of this potential. Dividing the CWT of the potential $\mathcal{W}_{\{\psi_a^n\}}\Delta\Phi$ by the average gravity at the Earth's surface leads to the CWT of the corresponding geoid.

APPENDIX C: SCALING FACTOR OF THE NORMALIZED SPECTRA

Here we describe the effect of the normalization of a wavelet spectrum with a background spectrum, and estimate the scaling factor that needs to be applied on the wavelet scales for the case of the backgrounds based on EGM2008 and Gebco oceanic geoids.

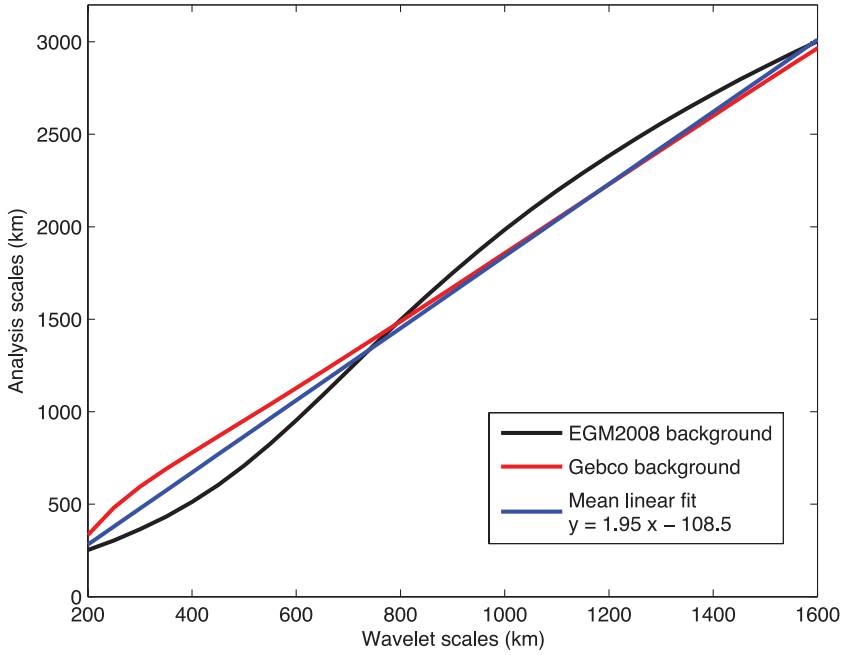

Figure C1. Analysis scales of normalized spectra after application of the scaling factor to the original wavelet scales, as a function of these original scales, for different kinds of background. Table of Poisson multipole wavelet and analysis scales. *Black curve*: case of a background based on EGM2008 geoid spectrum averaged over all oceans; *Red curve*: Case of a background based on the geoid effect of the Gebco bathymetry averaged over all oceans; *Blue line*: Average linear fit of the two previous curves, leading to the analysis scales used in the EGM2008/Gebco analysis of this paper.

Suppose the ideal case of a signal s, whose spherical harmonics spectrum only consists of contributions of degree ℓ_0, corresponding to the spatial resolution $d_0 = \frac{20000}{\ell_0}$ km. Let us denote $E_s(a)$ its Poisson wavelet spectrum, as a function of the wavelet scale a. It is a multiple of

$$\sum_m \left|\hat{\psi}_a^n(\ell_0, m)\right|^2 = \frac{2\ell_0+1}{4\pi}\frac{1}{4^n}(a\ell_0)^{2n}e^{-2a\ell_0}\left(\binom{2n}{n} + \mathcal{O}\left(\ell_0^{-1}\right)\right),$$

where $\hat{\psi}_a^n(l, m)$ stands for the spherical harmonics coefficient of degree l and order m of the Poisson wavelet ψ_a^n (Hayn & Holschneider 2009). The wavelet scale in kilometers is given by $20000\frac{a}{n}$ km, where n is the order of the Poisson wavelet. The maximum of the wavelet spectrum of s is obtained for the scale $\hat{a} = \frac{n}{\ell_0}$. Let us treat the background as a noise process in the sence that its spherical harmonics coefficients $\hat{n}_{lm}$ behave like

$$\langle \hat{n}_{lm} \rangle = 0, \quad \langle \hat{n}_{lm} | \hat{n}_{l'm'} \rangle = N_l \delta_{ll'} \delta_{mm'},$$

leading to a wavelet spectrum of

$$B(a) = 8\pi^2 \sum_l N_l \sum_m \left|\hat{\psi}_a^n(l, m)\right|^2.$$

The signal s superposed to this background results in the wavelet spectrum $E_s(a) + B(a)$. The spectrum relative to the background $B(a)$ is then, as a function of the wavelet scales a: $\frac{E_s(a)+B(a)}{B(a)}$.

We now look for the scale a_B, for which the normalized spectrum is maximal. Since the signal's spectrum fulfils $\partial_a E_s(a) = (\frac{2n}{a} - 2\ell_0)E_s(a)$, a_B verifies:

$$\left(\frac{2n}{a} - 2\ell_0\right) E_s(a)B(a) - E_s(a)\partial_a B(a)\Big|_{a=a_B} = 0 \qquad \text{(C1)}$$

For strictly positive values of the signal spectrum, on gets:

$$\frac{2n}{a_B} = \frac{\partial_a B(a)}{B(a)}\Big|_{a_B} + 2\ell_0. \qquad \text{(C2)}$$

If the background spectrum $B(a)$ is monotonically increasing, as in the case for the EGM2008 and Gebco geoid spectra, $a_B < \frac{n}{\ell_0}$ and the normalized wavelet spectrum is shifted towards smaller scales.

The eq. (C2) can be rearranged to

$$\hat{a} = \frac{n}{\frac{n}{a_B} - \frac{\partial_a B(a_B)}{2B(a_B)}} \qquad \text{(C3)}$$

with $\hat{a} = \frac{n}{\ell_0}$. This formula can be interpreted as follows: a signal of scale $\hat{a}$ (corresponding to $\hat{a} = \frac{n}{\ell_0}$ with the Fourier spectrum of the signal being centered around ℓ_0) has a maximum in the spectrum relative to the backgroung B at the scale a_B. In the general case, for an arbitrary background, one has to invert this equation numerically for a_B.

For the application with a normalization using EGM2008 and Gebco geoid spectra, we tried different models of the wavelet spectra of EGM2008 and Gebco geoids averaged over oceans. We finally approximate these spectra using polynomials of degree 5. These may thus include small effects of the searched geoid undulations, but our synthetic tests show that the impact on the scaling factor and scales of the undulations is small and can be neglected. The biased scales a_B obtained by solving eq. (C3), are finally represented in Fig. C1 as a function of the wavelet scales, for the EGM2008 and the Gebco geoid backgrounds. As the obtained scales are close, we apply an average linear fit of the two curves for deriving the analysis scales used in our study.

SUPPORTING INFORMATION

Additional Supporting Information may be found in the online version of this article:

Figure S1. Scale analysis of the geoid effect of Gebco bathymetry for the scales 1050 km and 1850 km. The azimuths of the dominant direction in the wavelet transform and the amplitudes of the wavelet transform at the dominant direction are shown.

Figure S2. Maps of dominant directions of wavelet transforms of the geoid model EGM2008 for the analysis scale 2600 km, with an amplitude threshold equal to 10 per cent (top panel) and 17 per cent (bottom panel) of the maximum CWT amplitude at this analysis scale. The amplitude masks are probably too selective, especially in the bottom panel, but they show that the NW-SE trend in the Pacific Ocean is robust.

Video Clip S1. The maps of the dominant directions of the wavelet transform of the geoid model EGM2008 for all calculated scales.

Video Clip S2. The maps of the dominant directions of the wavelet transform of the GEBCO bathymetry contribution to the geoid for all calculated scales.

Please note: Wiley-Blackwell are not responsible for the content or functionality of any supporting materials supplied by the authors. Any queries (other than missing material) should be directed to the corresponding author for the article.